

PERFORMANCE MEASUREMENTS ON A UAV-SCALE CYCLOIDAL ROTOR IN HOVER

A Thesis

by

ADAM JOHN KELLEN

Submitted to the Office of Graduate and Professional Studies of
Texas A&M University

in partial fulfillment of the requirements for the degree of

MASTER OF SCIENCE

Chair of Committee,	Moble Benedict
Committee Members,	John Valasek
	Edward White
	Sivakumar Rathinam
Head of Department,	Rodney Bowersox

May 2019

Major Subject: Aerospace Engineering

Copyright 2019 Adam John Kellen

ABSTRACT

This thesis discusses the optimization of a UAV-scale cycloidal rotors (or cyclorotor's) aerodynamic performance in hover through an extensive experimental parametric study and the development of a cyclocopter UAV. The current parametric study focused on collecting systematic time-averaged thrust and power measurements to characterize the effect of pitch kinematics and rotor geometry on the performance of a cyclorotor operating at Reynolds numbers between 100,000 and 300,000. Experiments were conducted for a range of rotational speeds across different blade pitch amplitudes for rotor configurations with varying airfoils, blade spans, chord-by-radius ratios, and number of blades. Based on the 37 unique rotor configurations, at an operating Reynolds number of 200,000, the optimal cycloidal rotor configuration had a chord-by-radius ratio of 0.66, 3 blades featuring a blade aspect ratio (span/chord) of 4 and a NACA 0020 airfoil, rotor aspect ratio (span/diameter) of 1.33 and cyclic pitch amplitude of $\pm 40^\circ$ and obtained a figure of merit of 0.6. The 17 lb. technology demonstrator prototype featured a dual-rotor configuration with cyclorotors featuring a novel split-blade design positioned at the front and rear of the vehicle. The vehicles rotors were designed based on the results from the parametric study. Flight performance was demonstrated through gimbal, tethered and free-flight tests.

DEDICATION

To my loving wife and parents who have constantly supported me

ACKNOWLEDGMENTS

I would like to begin by acknowledging and thanking my advisor Moble Benedict. I first met Dr. Benedict when I was a Junior looking for an opportunity to work and learn about academic research and what it meant to be a graduate student. Even as an undergraduate, he pushed me to take ownership of my own project and participate in the summer research program (USRG). Both experiences proved instrumental in my selection as an outstanding senior engineer in 2016 and my eventual decision to attend graduate school. Now over all of the years I have spent in the Advanced Vertical Flight Lab I have been exposed to numerous projects and learned more than I ever would of considered possible. It has been a pleasure and honor to work and learn under Dr. Benedict and I could not have asked for a better mentor.

A special acknowledgement and thank you for all of the students, professors and staff at Texas A&M University and especially those in the Aerospace Engineering department. Between the amazing advisers, business staff, secretaries and professors I always felt welcomed and appreciated. The sense of family in the department is unmatched and I could not of asked for a better place to spend my collegiate career. A special thank you to Dr. John Valasek, Dr. Edward White, and Dr. Sivakumar Rathinam for agreeing to serve on my committee.

I would remiss if I didn't thank each and every one of my fellow coworkers in the Advanced Vertical Flight Lab. Spending everyday down in the basement working would not of been half as memorable or rewarding without you. Whether is consulting about a question or problem with my research or debating current events and politics everyday in the lab was a new adventure that I will not soon forget. A special thanks to the two undergraduate students, Joel White and Matthew Kendall, who dedicated countless hours to assisting me with my projects.

My family deserves the biggest thanks of all as nothing that I accomplished would have been possible without them. My parents instilled in me the discipline and values I needed to be successful in engineering. Beyond that they provided me with everything I needed to nurture my love for science and technology as a kid and have continued that support throughout my collegiate

career. My brothers and sister were always calling to check in on my progress and encourage me to fight through the problems that arose in my research. My loving wife, Victoria, has always been my rock and constant source of encouragement. No matter how school and research was going, I was blessed to be able to come home to her and could not of asked for a better partner to go through it all with.

I would like to end by taking a moment to thank everyone else I interacted with in the last seven years who I may have missed mentioning above. Individuals from across the university and across the country have supported me and my work and I am deeply thankful for the roles they have played.

CONTRIBUTORS AND FUNDING SOURCES

Contributors

This work was supported by a thesis committee consisting of Professor Moble Benedict (advisor), Professor John Valasek and Professor Edward White of the Department of Aerospace Engineering and Professor Sivakumar Rathinam of the Department of Mechanical Engineering.

Undergraduate research assistants, Joel White and Matt Kendall, provided assistance during the parametric study presented in Chapter 3. The design for the flight controller utilized on the demonstration vehicle presented in Chapter 4 was completed by Dr. Vikram Hrishikeshavan from the department of Aerospace Engineering at the University of Maryland.

All other work conducted for the thesis was completed by the student independently.

Funding Sources

Graduate study was supported under a grant from the Army/Navy/NASA sponsored Vertical Lift Research Center of Excellence (VLRCE) led by the University of Maryland (Grant Number - 46731-Z8458101). Dr. Mahendra Bhagawat serves as the Technical Monitor.

NOMENCLATURE

A	Rectangular projected area, $(b \times 2R)$, m^2
A_S	Blade swept area, $2\pi Rb$, m^2
b	Blade span, m
c	Blade chord length, m
c/R	Chord-by-Radius ratio
C_P	Power coefficient, $P/\rho A(\Omega R)^3$
C_Q	Power coefficient, $Q/\rho AR(\Omega R)^2$
C_T	Power coefficient, $T_{Res}/\rho A(\Omega R)^2$
D	Diameter, m
DL	Disk loading, T_{Res}/A , $\frac{N}{m^2}$
FM	Figure of merit
L_1, L_2, L_3, L_4	Linkage lengths of the four-bar pitch mechanism
N_b	Number of blades
P	Total aerodynamic power, $Q\Omega$, W
PL	Power loading, T_{Res}/P , $\frac{N}{W}$
Q	Aerodynamic torque, Nm
R	Radius, m
T_{Res}	Resultant thrust, $\sqrt{T_Y^2 + T_Z^2}$, N
T_Z	Rotor vertical thrust, N
T_Y	Rotor sideward thrust, N
ρ	Air density, $\frac{kg}{m^3}$
σ	Rotor solidity, $N_b c / 2\pi R$
Φ	Thrust angle, $\tan^{-1} \left(\frac{T_Y}{T_Z} \right)$, Deg

ψ	Azimuthal position of blade, <i>Deg</i>
Ω	Rotational speed of rotor, <i>RPM</i>

TABLE OF CONTENTS

	Page
ABSTRACT	ii
DEDICATION	iii
ACKNOWLEDGMENTS	iv
CONTRIBUTORS AND FUNDING SOURCES	vi
NOMENCLATURE	vii
TABLE OF CONTENTS	ix
LIST OF FIGURES	xi
LIST OF TABLES.....	xiv
1. INTRODUCTION.....	1
1.1 Cycloidal Rotor Operating Principle	1
1.2 Literature Review	2
1.3 Research Objectives.....	7
2. EXPERIMENTAL PROCEDURE	8
2.1 Cycloidal Rotor Hover Test Stand.....	8
2.1.1 Rotor Design.....	11
2.1.1.1 Blade Design	12
2.1.1.2 Pitch Mechanism	13
2.1.1.3 Support Structure and Transmission.....	15
2.1.2 Tested Configurations	16
2.2 Data Collection and Processing	18
3. PARAMETRIC STUDY	19
3.1 Aerodynamic Measurements	20
3.1.1 Cyclorotor Forces	20
3.1.2 Power Analysis	22
3.2 Rotor Parameters	23
3.2.1 Virtual Camber	23
3.2.2 Effect of Blade Cyclic Pitching Amplitude	25

3.2.3	Effect of Blade Airfoil Thickness.....	30
3.2.4	Effect of Blade Span (Blade Aspect Ratio)	33
3.2.5	Effect of Chord-by-Radius Ratio	36
3.2.6	Effect of Number of Blades	41
3.2.7	Effect of Rotor Solidity	44
3.3	Optimal Geometry	47
3.4	Concluding Remarks.....	48
4.	TECHNOLOGY DEMONSTRATOR PROTOTYPE	50
4.1	Vehicle Design	50
4.1.1	Rotor Design.....	53
4.1.1.1	Rotor Geometry and Blade Kinematics	53
4.1.1.2	Pitch Mechanism	55
4.1.1.3	Blade Design	56
4.1.1.4	Rotor Support Structure and Transmission.....	58
4.2	Attitude Control Strategy	59
4.2.1	Avionics and Feedback Control.....	61
4.3	Experimental Testing	62
4.4	Concluding Remarks.....	64
5.	SUMMARY AND CONCLUSIONS	65
5.1	Future Work	67
	REFERENCES	69

LIST OF FIGURES

FIGURE	Page
1.1 Cyclorotor concept	2
1.2 Kirsten's cyclorotor study.	3
1.3 Bosch Aerospace cyclorotor.	4
1.4 MAV-scale cyclocopters.....	5
1.5 PL vs DL : MAV-scale cyclocopter and conventional rotor	5
1.6 Power vs. Forward Speed: trimmed flight of MAV-scale cyclorotor	6
1.7 Seoul National University cyclocopters.	6
2.1 Cyclorotor blade coordinates	8
2.2 Cycloidal rotor hover test stand: 3-component balance	9
2.3 Hover stand configurations.....	9
2.4 Force balance.	10
2.5 Torque balance.....	11
2.6 Hover stand cyclorotor design.	11
2.7 Cyclorotor blade design.	13
2.8 Manufactured blades for parametric study.	13
2.9 Hover stand cyclorotor pitch mechanism.....	14
2.10 L_3 and L_2 links.	14
2.11 Hover stand cyclorotor structure.....	15
2.12 Hover stand support arms.	16

2.13 Hover stand LabVIEW VI	18
3.1 Cyclorotor area definitions.....	19
3.2 Thrust vs. RPM: 2-bladed cyclorotor. $c/R = 0.26$, $PA = \pm 30^\circ$	21
3.3 Thrust vs. RPM: 6-bladed cyclorotor. $c/R = 0.66$, $PA = \pm 30^\circ$	21
3.4 Power vs. RPM: 2-bladed cyclorotor. $c/R = 0.26$, $PA = \pm 30^\circ$	23
3.5 Power vs. RPM: 6-bladed cyclorotor. $c/R = 0.66$, $PA = \pm 30^\circ$	23
3.6 Virtual camber effect.	24
3.7 PL vs. DL : 2-bladed cyclorotor. $c/R = 0.66$, varying symmetric pitch amplitudes ...	26
3.8 PL vs. DL : 4-bladed cyclorotor. $c/R = 0.66$, varying symmetric pitch amplitudes ...	26
3.9 PL vs. DL : 2-bladed cyclorotor. $c/R = 0.66$, varying asymmetric pitch amplitudes .	27
3.10 PL vs. DL : 4-bladed cyclorotor. $c/R = 0.66$, varying asymmetric pitch amplitudes .	28
3.11 Optimal Pitch Amplitude vs. Chord-by-Radius Ratio: 2-bladed cyclorotor	29
3.12 Optimal Pitch Amplitude vs. Number of Blades: varying chord-by-radius ratio	30
3.13 C_T vs. Pitch Amplitude: varying airfoil thickness	31
3.14 C_P vs. Pitch Amplitude: varying airfoil thickness	32
3.15 PL vs. DL : varying airfoil thickness	33
3.16 C_T/σ vs. AR : varying chord-by-radius and pitch amplitude	34
3.17 C_P/σ vs. AR : varying chord-by-radius and pitch amplitude	34
3.18 PL vs. AR for fixed disk loading: varying chord-by-radius and pitch amplitude	35
3.19 2-bladed cyclorotor with elliptical endplate	36
3.20 PL vs. DL : 2-bladed cyclorotor with and without endplate	36
3.21 Φ vs. c/R : varying pitch amplitude	38
3.22 Thrust vs. c/R : varying pitch amplitude.....	39
3.23 Power vs. c/R : varying pitch amplitude	39
3.24 PL vs. c/R for fixed disk loading: varying pitch amplitude	41

3.25 C_T/σ vs. Nb for fixed disk loading: varying chord-by-radius ratio and pitch amplitude	42
3.26 C_P/σ vs. Nb for fixed disk loading: varying chord-by-radius ratio and pitch amplitude	43
3.27 PL vs. Nb for fixed disk loading: varying chord-by-radius ratio and pitch amplitude	44
3.28 C_T/σ vs. σ : varying rotor configuration	45
3.29 C_T/σ vs. σ : varying rotor configuration	46
3.30 PL vs. σ : varying rotor configuration	47
3.31 FM vs. σ : optimal pitch kinematics for every rotor configuration.....	48
3.32 Optimal cyclo rotor configuration.....	48
4.1 Cyclocopter concept	51
4.2 17 lb cyclocopter pictured with 29 g cyclocopter.....	51
4.3 Vehicle cyclo rotor performance.	55
4.4 Four-bar pitch mechanism: Schematic and vehicle.	56
4.5 Technology demonstrator blade design.....	58
4.6 Cyclo rotor structure and transmission.....	59
4.7 Control definitions.....	60
4.8 Attitude control strategy.....	61
4.9 Motor reaction torques effect on pitch stability. Pitch up maneuver represented.	61
4.10 Feedback loop.	62
4.11 Gimbal test stand.	63
4.12 Tethered flight test	63
4.13 Free flight test	64

LIST OF TABLES

TABLE	Page
2.1 Tested configurations.	17
4.1 Design specifications for cyclocopter.....	52
4.2 Weight breakdown for cyclocopter.	52

1. INTRODUCTION

Unmanned Air Vehicles (UAVs) are a key technology shaping the future. They are capable of accomplishing tasks that were previously too difficult, costly, or unsafe to complete from the ground or via manned aircraft. Creating the next generation of vertical takeoff and landing (VTOL) capable UAVs requires revolutionary vehicle concepts. Traditionally these concepts would rely on conventional rotors/propellers as their primary means of propulsion. Unfortunately, conventional rotors tend to suffer from high susceptibility to gust disturbances and high acoustic signatures. A cycloidal rotor (or cyclorotor) is a revolutionary horizontal-axis propulsion system which is capable of near instantaneous thrust vectoring about the rotor azimuth. Cyclorotors are now being investigated as an alternative propulsion system for larger UAVs. The work presented in this thesis involves the experimental optimization of a UAV-scale cyclorotor's aerodynamic performance and the creation of a technology demonstrator vehicle.

1.1 Cycloidal Rotor Operating Principle

A cycloidal rotor, or cyclorotor, is a rotary-based propulsion system consisting of multiple blades rotating about an offset horizontal axis (Fig. 1.1a). Each blade can rotate about its pitch axis with the span positioned parallel to the axis of rotation. To create a net vertical force, the blades are cyclically pitched in a 1/rev fashion such that the blades experience positive geometric angles of attack during both the top and bottom halves of its circular trajectory (Fig. 1.1b). The magnitude and direction of the net thrust vector can be changed by varying the amplitude and phase of the cyclic blade pitch kinematics.

Compared to traditional rotary systems the cyclorotor provides several unique advantages. Aerodynamically, each span-wise blade element of a cyclorotor operates at similar aerodynamic conditions, thus tending to show that the blades can be easily designed to maximize thrust and aerodynamic efficiency. The cyclic pitching kinematics combined with the high blade pitch rates combined delays the onset of blade stall further augmenting the thrust generation of the cyclorotor.

Furthermore, the ability to instantaneously vary the magnitude and direction of the net thrust vector can provide high control authority for cyclorotor-based aircraft, referred to as "cyclocopters", compared to multirotor based systems.

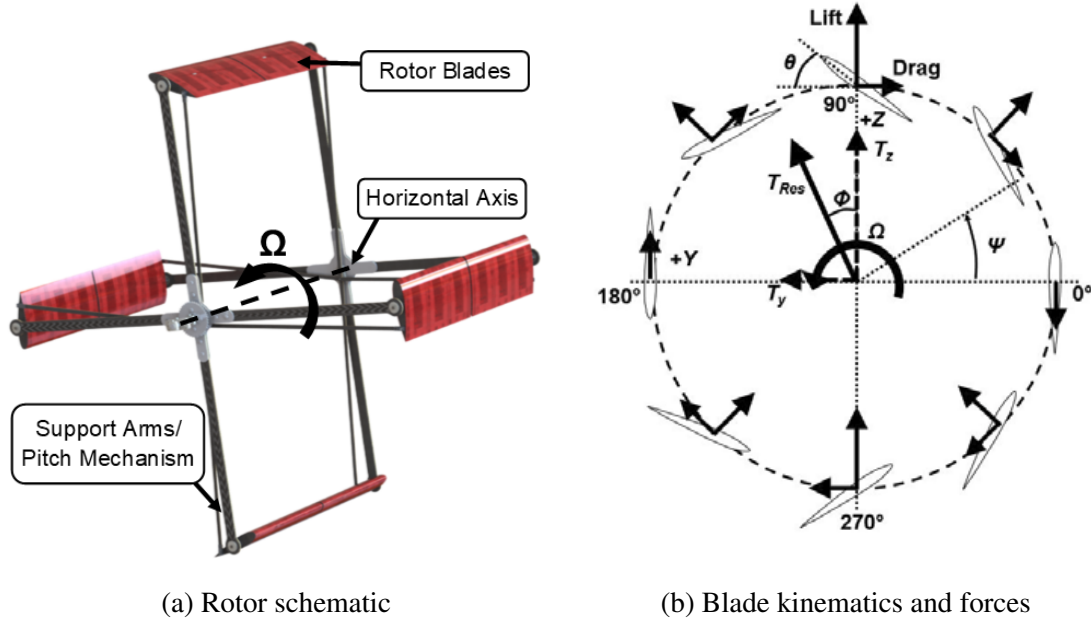


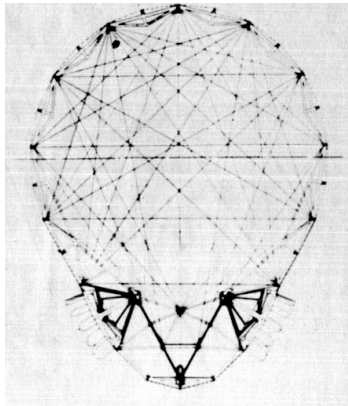
Figure 1.1: Cyclorotor concept

1.2 Literature Review

The cyclorotor concept originated in the early 20th century [1]. Many of the earliest attempts failed to achieve much success due to structural and aerodynamic challenges. Interest in cyclorotors quickly lessened with the successful demonstration of conventional helicopters, but scientific studies continued due to the benefits a cyclorotor system could provide. The current section discusses many of scientific studies that were conducted on cyclorotors since the 1920s.

One of the earliest significant scientific studies on cyclorotors was conducted in the 1920s by Professor Kurt Kirsten at the University of Washington [2, 3]. The study was conducted as part of an engineering effort with Boeing with the goal of constructing a cyclorotor for an airship followed by the creation of a "cycloplane" (Fig. 1.2). Several generations of cyclorotors were designed and tested in preparation for full-scale testing. Unfortunately, the airship designated to be used for the full-scale testing crashed before testing could be completed leading to the indefinite suspension of

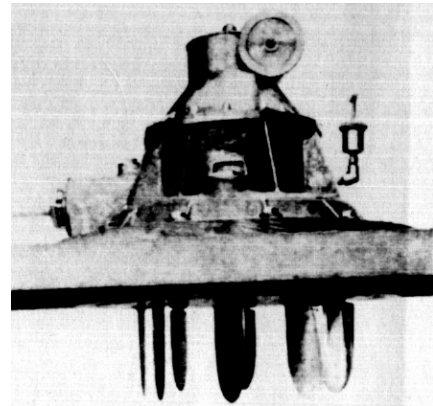
study. With suspension of the air vehicle testing the cyclorotor design was modified to be used as a ship propeller (Fig. 1.2c). The resulting rotor was integrated into a ship and extensively tested with travel distances totaling 4000 nautical miles. This initial design was improved over the coming decades into the voith-schneider propeller which remains the only commercial application of the cyclorotor to date [4].



(a) Cyclorotor driven airship



(b) Cycloplane



(c) Ship cyclopropeller

Figure 1.2: Kirsten's cyclorotor study.

Between 1924 and 1933, Strandgren conducted a series of experimental studies and the first ever computational study of the aerodynamics of a cyclorotor [5]. During his experiments he created and tested a full scale cyclorotor system, but the real advance came as part of his computational work. Through his work the first ever aerodynamic model was created to predict the thrust of a cyclorotor system.

During the same time period, John Wheatley at the Langley Memorial Aeronautical Laboratory conducted his own experimental and analytical studies [6, 7]. Wheatley levered his analytical study to examine the feasibility of the cyclorotor for manned aircraft. Based on the results it was determined that aerodynamically the system is sound, but there are large structural challenges that must be addressed. For Wheatley's experimental study, he tested a cyclorotor with an 8 ft. diameter and span in the NACA 20 ft. wind tunnel at advanced ratios between 0.2 and 0.5. The experimental results and the differences found from the analytical results demonstrated the need to properly account for the highly unsteady nature of a cyclorotors aerodynamics to accurately

predict performance. Unsteady aerodynamics were not fully understood at that time and would not be integrated into analytical studies until much later.

The onset of World War 2 and the lack of successful demonstrations of cyclorotor based vehicle led to a significant reduction in the number of studies conducted following the work of Strandgren and Wheatley. The development of advanced composite material and expanded interest in unmanned aerial vehicles led to the reemergence of interest in the study of cyclorotors in the late 1990s. In response to a request for an innovative propulsion system Bosch Aerospace proposed the use of a cyclorotor for a 600 lb UAV [8, 9]. Experimental and analytical studies were conducted with large improvements in both areas, but unfortunately flight was never demonstrated (Fig. 1.3).



(a) Test rotor



(b) UAV concept

Figure 1.3: Bosch Aerospace cyclorotor.

Entering into the 21st century pioneering research on cyclorotors has been conducted at the University of Maryland, Texas A&M University, and Seoul National University. Work conducted at the University of Maryland and Texas A&M University focused on the development micro air vehicle (MAV) scale cyclorotors. Their research has resulted in the creation of cyclocopters between 29 and 800 grams (Fig. 1.4) [10, 11, 12]. The research established a fundamental understanding of the aeromechanics of MAV-scale cyclorotors. Systematic performance measurements at MAV scales demonstrated higher hover efficiency than a conventional rotor because of uniform aerodynamic loading along blade span and favorable unsteady aerodynamic phenomena (Fig. 1.5) [13, 14, 15, 16]. Wind tunnel studies showed the cyclorotor is capable of efficient high-speed forward flight even beyond an advance ratio of 1.0 by phasing its cyclic pitch, essentially thrust

vectoring (Fig. 1.6) [17, 18, 19]. Thrust vectoring capability means a cyclocopter can transition from hover to high-speed forward flight without any configuration change [20].

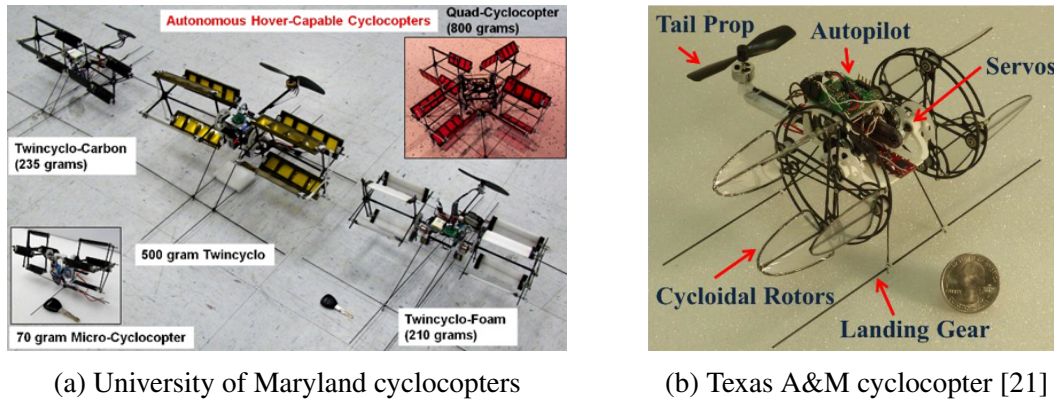


Figure 1.4: MAV-scale cyclocopters.

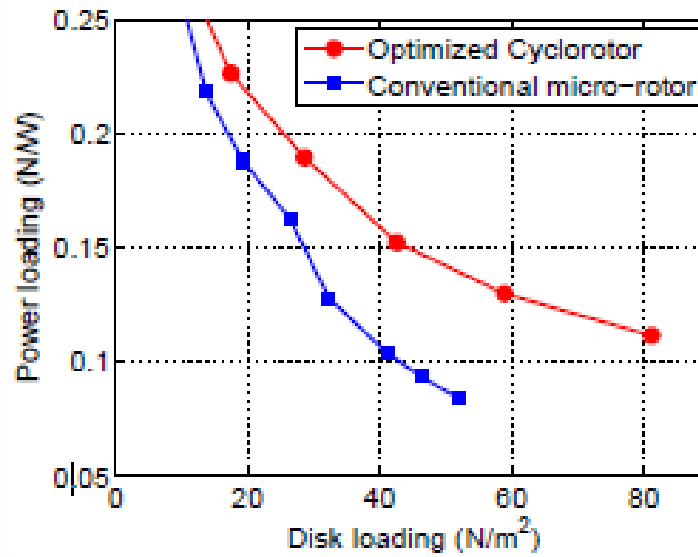


Figure 1.5: PL vs DL : MAV-scale cyclocopter and conventional rotor [13]

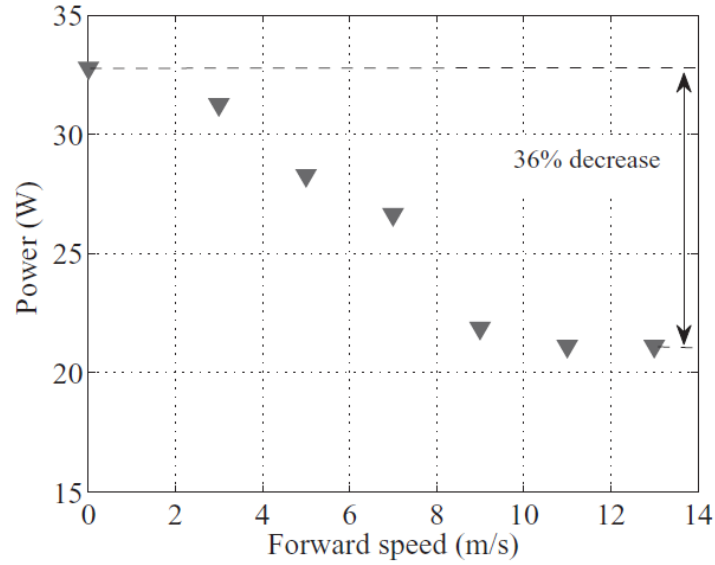


Figure 1.6: Power vs. Forward Speed: trimmed flight of MAV-scale cyclorotor [19]

Work conducted at Seoul national university focused on the creation of UAV-scale cyclorotors ranging between 10 kg and 110 kg [22, 23, 24, 25]. Prior to the design of the vehicles a multi-disciplinary optimization problem was solved computationally to determine the design capable of producing the maximum thrust for the defined power. The results were used in the construction of multiple cyclocopters. The two vehicles which have achieved stable flight are a dual rotor cyclocopter with a conventional tail propeller and a four rotor cyclocopter (Fig. 1.7).



(a) Dual-rotor cyclocopter tethered flight [25]



(b) Four rotor cyclocopter free flight [26]

Figure 1.7: Seoul National University cyclocopters.

1.3 Research Objectives

The study presented here represents an extension of previous research regarding UAV-scale cyclorotors. Previous UAV-scale studies successfully demonstrated vehicle flight, but lacked sufficient scientific studies to determine the optimal rotor geometry. The previous study was conducted analytically with minimal experimental validation and focused on determining a configuration which would produce the maximum thrust for the available engine power. The study was a significant first step, but the study set parameter boundaries that were too narrowed to definitively state the optimal configuration nor determine the effect each geometric parameter has on aerodynamic performance. The current study will include a systematic experimental study to quantify the effect of each geometric parameter (airfoil thickness, blade aspect ratio, chord-by-radius ratio, number of blades, and rotor solidity) and pitch kinematics on thrust generation and aerodynamic efficiency. The results of the experimental study will be used in the construction and demonstration of an optimized UAV-scale cyclocopter.

2. EXPERIMENTAL PROCEDURE

The goal of the current experimental study is to characterize the effect of a cyclorotor's rotor geometry and pitch kinematics on aerodynamic performance in hover. To conduct this study a state-of-the-art hover stand featuring a three-component force balance was designed and built in-house. The cyclorotor models tested in the experimental study were developed to simplify changes in geometric parameters while maintaining high stiffness-to-weight ratios. Time-averaged data measurements were conducted to characterize aerodynamic performance of each rotor configuration.

2.1 Cycloidal Rotor Hover Test Stand

The hover stand was designed to measure vertical thrust (T_Z), sideward thrust (T_Y), aerodynamic torque (Q), and rotational speed. From these measurements, the resultant thrust (T_{Res}) magnitude and direction (acting at an angle Φ as shown in Fig. 2.1), aerodynamic power (P) and relevant performance metrics can be obtained. The hover stand was created from a support frame and force/torque balance sub-assemblies (Fig. 2.2).

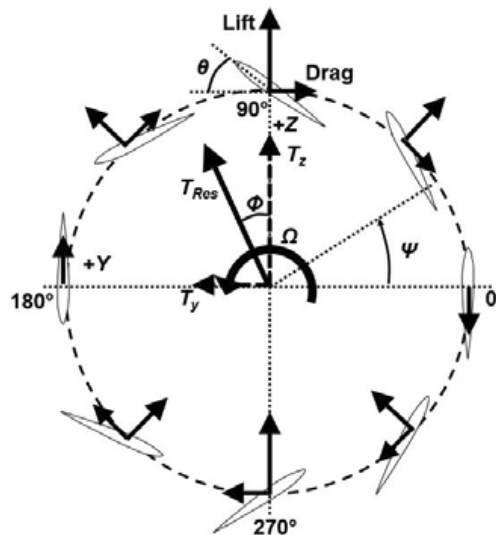


Figure 2.1: Cyclorotor blade coordinates

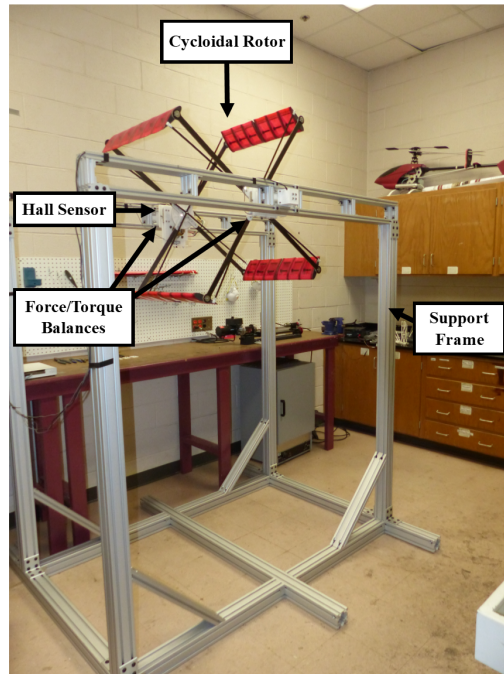
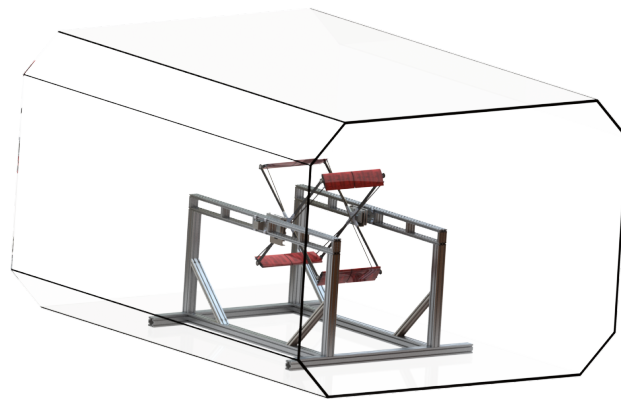


Figure 2.2: Cycloidal rotor hover test stand: 3-component balance

The support frame was created using pre-fabricated 80-20 extrusions. The extrusions simplified manufacturing and provided flexibility for testing various rotor spans. The frame's base could also be reassembled to provide two separate test heights, one ideal for hover testing (Fig. 2.3a) and one ideal for wind tunnel testing in the Oran W Nicks low speed wind tunnel at Texas A&M University (Fig. 2.3b) [27].



(a) Tall configuration



(b) Wind tunnel configuration

Figure 2.3: Hover stand configurations.

The force balance design featured a series of load plates machined from Delrin mounted to linear bearings and fixed in place by load cells (Fig. 2.4). Linear bearings with a coefficient of friction of 0.003 (Tusk BX5-2) were used in the Y and Z direction. The bearings created the freedom of movement and load path in one direction for each individual plate while transferring the remaining forces and torques. The load cells feature a 25 lbs (111 N) limit (Transducer Techniques MLP-25). The load cells were calibrated after mounted to account for frictional losses in the linear bearings. The primary and secondary force balances feature similar designs except for the larger front plate used for mounting the driving motor and the Hall-effect sensor, which generated a 4/rev signal to measure rotational speed.

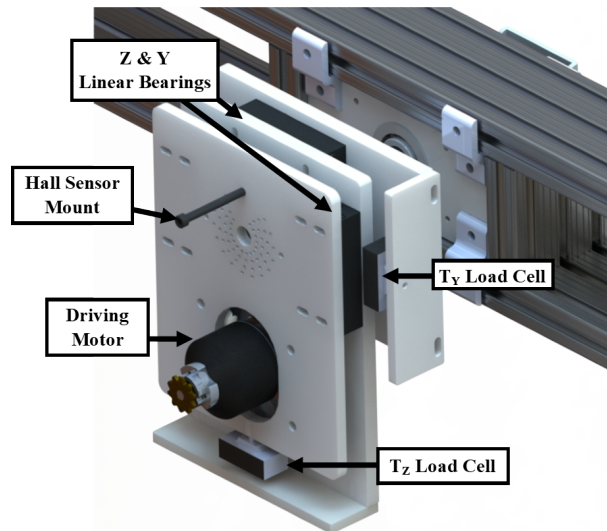


Figure 2.4: Force balance.

The torque balance assembly features the force balance assembly mounted on a D-rod through two rotational bearings (Fig. 2.5). The 3/4" aluminum D-rod transfers all forces in the Y and Z directions (Fig. 2.1) through the rotational bearings mounted in the support frame. Rotational movement is restricted by the torque cell with a 200 in-lb (22.6 N-m) limit (Transducer Techniques TRT-200). Similar to the load cells, the torque cell is calibrated, once mounted on the frame, to account for frictional losses in the bearings.

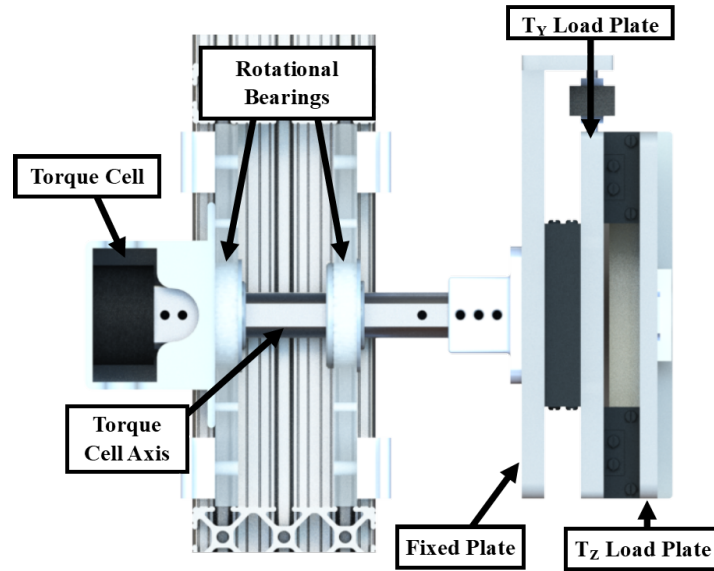


Figure 2.5: Torque balance.

2.1.1 Rotor Design

The cyclorotor used for the parametric study was designed to be versatile for testing numerous rotor configurations and simple to manufacture. Transverse centrifugal loads in excess of 100gs creates the need for all components to be designed with high strength to weight ratio. The primary elements of the structure are the rotor blades, pitch control arms and support structure (Fig. 2.6).

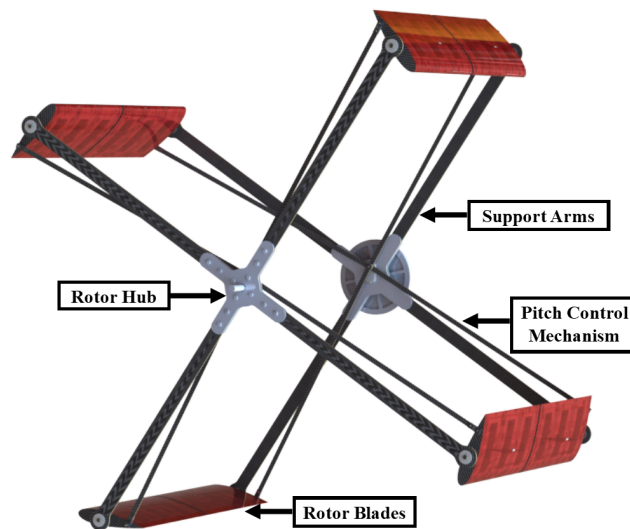


Figure 2.6: Hover stand cyclorotor design.

2.1.1.1 Blade Design

Cyclorotor blades must be carefully designed to ensure durability and functionality in the presence of the centrifugal and aerodynamic loads. The high centrifugal loads on a cyclorotor introduce large transverse bending loads. Aerodynamic loads do not exceed the combined lift and drag on each of the blades meaning their contribution to blade deformation is minimal compared to the centrifugal loads. To that end the blades are designed primarily accounting for the centrifugal loads meaning the primary goal is to maximize the blade's stiffness-to-weight ratio.

The blade design was improved and modified with the manufacturing of each blade, however each blade design was based on an assembly of blade ribs, filler foam, and composite tubes (Fig. 2.7). The blade ribs were cut from a carbon fiber laminate structure with a foam core (Fig. 2.7a). The material provides a high strength to weight ratio with the only compromise being reduced compressive strength and a laminated structure. In the split blade design, a 1mm thick aluminum ring was machined and pressed into every rib to provide a mounting surface for the roller bearings that transferred loads to the entire rib structure. The filler space between the ribs is filled with low-density Rohacell foam assemblies (Fig. 2.7b). The foam formed the outer shape of the blade and provided a continuous surface for mounting the mylar (Monokote[®]) cover. The foam provides minimal bending strength so its weight was severely limited through the removal of large portions of the material in the center of each rib structure. Since epoxy is heavy, the larger leading edge pieces of the filler foam are connected using wooden dowel pins to reduce weight. The main structural rod and pitching axis running between the side supports is a 3/8" pultruded carbon fiber tube. Smaller 3/16" carbon fiber tubes run through the rear of each blade (Fig. 2.7c). The rods provide additional structural stiffness as well as the mounting point for the rear pitch control rod. Nylon spacers on each side of the solid blades, or blade halves in the split blade, prevent any pinching between the blades or supports. In total, 9 different types of blades were manufactured with multiples of each blade type created, equating to a total of 26 blades (Fig. 2.8).

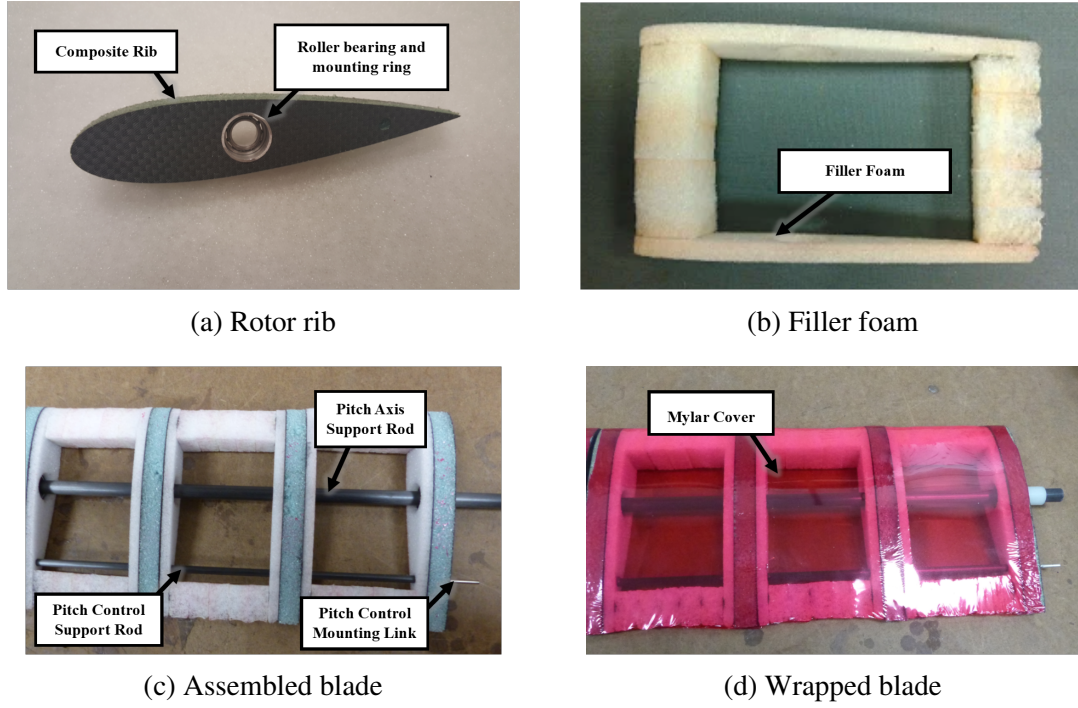


Figure 2.7: Cyclorotor blade design.



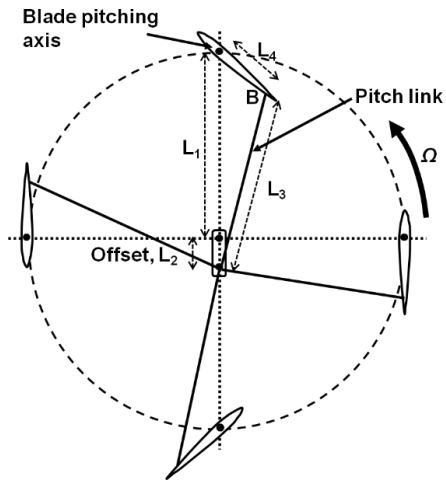
Figure 2.8: Manufactured blades for parametric study.

2.1.1.2 Pitch Mechanism

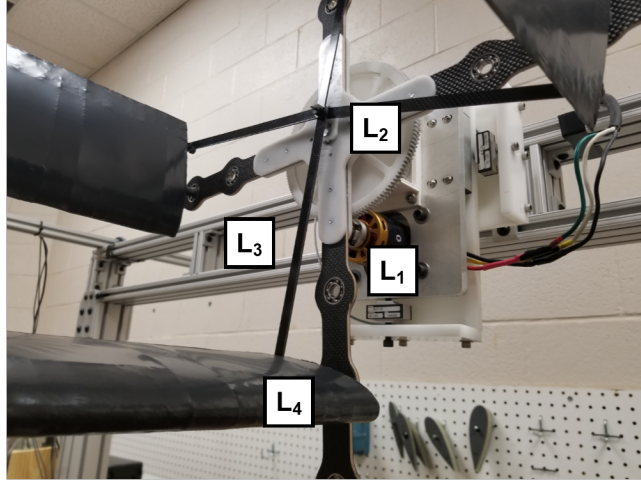
The pitch control mechanism developed for use on the cyclorotor must be capable of accurately generating the desired pitch kinematics while being simple to manufacture. The pitch mechanism design was created using a four-bar linkage due to its ability to kinematically couple pitch kinematics to rotor rotation (Fig. 2.9a).

The four bar mechanism was recreated using four fixed lengths (Fig. 2.9b). The rotor radius (support arms) serves as L_1 . A machined Delrin link serves as the primary control link (L_2). L_3 is the pitch control link which transfers the required forces to achieve cyclic pitching and was created

using one of two methods depending on the link length (Fig. 2.10). The three longest pitch links were machined from a 1/16" birch carbon fiber laminate with a machined Delrin fork link at the connection point between the rotor blades and offset link. The remainder of the pitch links were machined from a 1/16" carbon fiber plate. The distance between the blade pitch axis and the pitch link (L_3) mounting point serves as L_4 .



(a) Schematic



(b) Hover stand

Figure 2.9: Hover stand cyclorotor pitch mechanism.

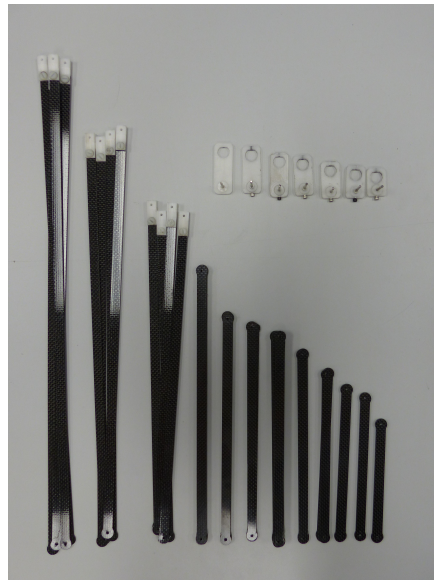


Figure 2.10: L_3 and L_2 links.

2.1.1.3 Support Structure and Transmission

The rotor support must be capable of withstanding the large tension loads resulting from the centrifugal loads on the blades. To ensure the rotor is capable of handling the large loads with minimal deflection and to minimize rotor weight, the support arms were machined from a 5/32" thick laminate composite material (Fig. 2.11). The carbon fiber laminate features a birch core and is capable of handling both the large tension loads and any compressive loads caused during handling. Roller bearings were pressed into the mounting points to provide a rotational degree of freedom for the fixed blade designs. To provide configuration flexibility the support arms were sandwiched in the center hub, which was created from two Delrin plates. The hub allowed experimenting with differing numbers of blades as well as replacing the support arms with the desired length (Fig. 2.12). The rotor support structure was driven via a spur-gear based transmission system with a gear ratio of 7.78:1 and a driving motor. The design ensured the electric motor would operate at its efficient high-speed low-torque condition.

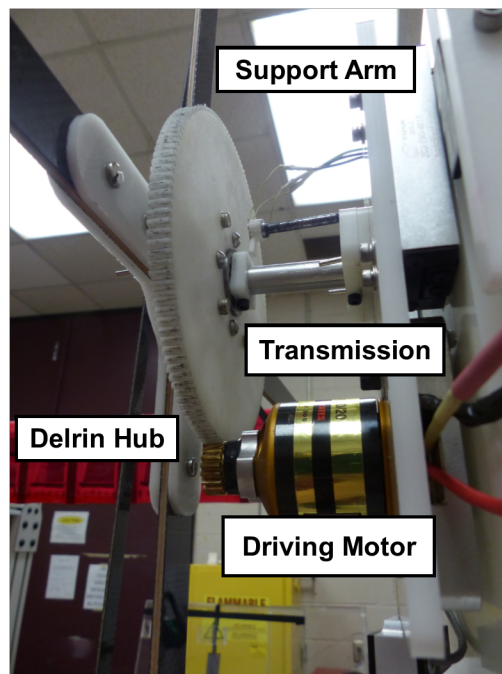


Figure 2.11: Hover stand cyclorotor structure.



Figure 2.12: Hover stand support arms.

2.1.2 Tested Configurations

During the experimental parametric study a total of 37 unique degree configurations were tested. Each of these configurations was tested at cyclic pitch amplitudes of $\pm 15^\circ$ $\pm 20^\circ$ $\pm 25^\circ$ $\pm 30^\circ$ $\pm 35^\circ$ and $\pm 40^\circ$. Two of the configurations (#6 and #9) were tested with additional asymmetric cyclic pitch amplitudes and one configuration (#24) was tested with elliptical endplates. In total, 234 unique combinations of geometric configurations and pitch kinematics was tested. Table 2.1 provides a summary of the geometric parameters of all of the rotor configurations tested.

#	c(in)	Nb	R(in)	b(in)	Airfoil
1	5.5	2	5.5	22	NACA0020
2	5.5	2	6.0	22	NACA0020
3	5.5	2	6.66	22	NACA0020
4	5.5	2	7.5	22	NACA0020
5	5.5	2	8.25	16.5	NACA0020
6	5.5	2	8.25	22	NACA0020
7	5.5	2	8.25	27.5	NACA0020
8	5.5	3	8.25	22	NACA0020
9	5.5	4	8.25	22	NACA0020
10	5.5	5	8.25	22	NACA0020
11	5.5	6	8.25	22	NACA0020
12	5.5	2	9.17	22	NACA0020
13	5.5	2	11.0	16.5	NACA0020
14	5.5	2	11.0	22	NACA0020
15	5.5	2	11.0	27.5	NACA0020
16	5.5	3	11.0	22	NACA0020
17	5.5	4	11.0	22	NACA0020
18	5.5	5	11.0	22	NACA0020
19	5.5	6	11.0	22	NACA0020
20	5.5	2	13.33	22	NACA0020
21	5.5	2	16.66	22	NACA0020
22	5.5	2	20.0	22	NACA0020
23	5.5	2	21	22	NACA0015
24	5.5	2	21	22	NACA0020
25	5.5	2	21	22	NACA0025
26	5.5	3	21	22	NACA0020
27	5.5	4	21	22	NACA0020
29	5.5	5	21	22	NACA0020
30	5.5	6	21	22	NACA0020
31	8.0	2	5.5	22	NACA0020
32	8.0	2	8.25	22	NACA0020
33	8.0	2	11.0	22	NACA0020
34	8.0	2	13.33	22	NACA0020
35	8.0	2	16.66	22	NACA0020
36	8.0	2	20.0	22	NACA0020
37	10.0	2	13.33	22	NACA0020

Table 2.1: Tested configurations.

2.2 Data Collection and Processing

Voltage measurements from the load cells, torque cells and Hall-effect sensors was collected using a National Instruments data acquisition (DAQ) input board. The DAQ acquired 2000 samples over 2 seconds at a 1 KHz sampling rate before passing it to the computer to be processed in the LabVIEW software. The LabVIEW software provided the interface necessary for determining the reference measurement for zero load on the load and torque sensors, averaging the data over the extended time, and processing the Hall-effect sensor data to equate it to a rotational speed (Fig. 2.13). Experimental data points were taken as an average of 8 seconds worth of samples. Experiments were repeated three times for each configuration to ensure repeatability in results. The respective data files were then post-processed using MATLAB. The large volume of data led to the use of multiple data organization and manipulation techniques to ensure accurate processing and plotting.

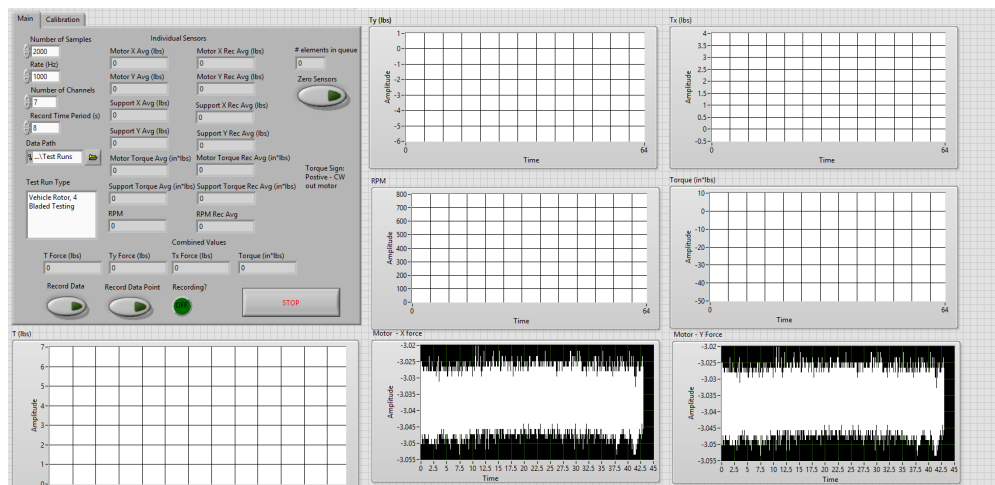


Figure 2.13: Hover stand LabVIEW VI

3. PARAMETRIC STUDY

A systematic experimental parametric study has been conducted on the UAV-scale cyclorotor by varying blade kinematics and rotor geometry to investigate their effect on cyclorotor performance in terms of both thrust and aerodynamic efficiency, quantified in terms of both power loading (thrust/power) and figure of merit (FM) [28, 29, 30]. Unlike traditional rotors, cyclorotors have differing swept and projected areas, thus non-dimensionlized parameters, C_T , C_P , and FM , and disk loading (thrust/area), are calculated based on the projected rectangular area perpendicular to the resultant thrust vector ($A = Db$) while rotor solidity, σ , is calculated using the swept area ($A_s = \pi Db$) (Fig. 3.1). The following sections provide a detailed discussion on the method undertaken for aerodynamic force and power power measurements, the effect of various rotor parameters on aerodynamic performance and the optimal rotor geometry.

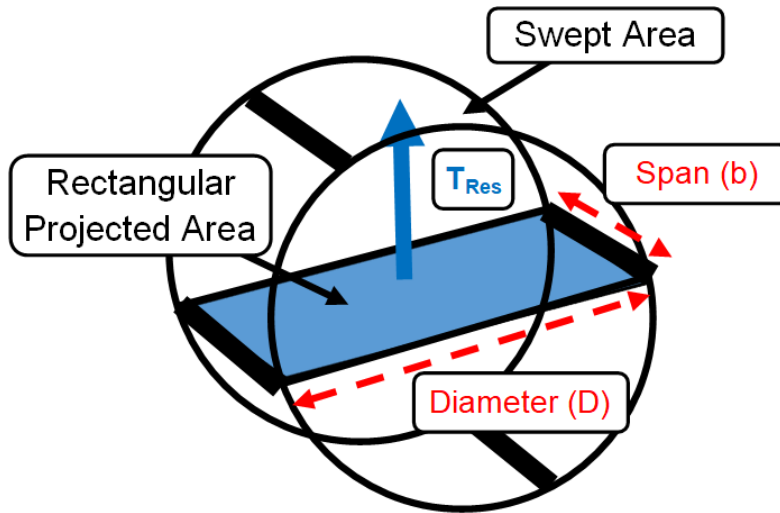


Figure 3.1: Cyclorotor area definitions

3.1 Aerodynamic Measurements

3.1.1 Cyclorotor Forces

The fixed frame coordinates utilized in the force measurements are shown in Fig. 2.1. T_Z is the vertical force and T_Y is the sideward force. The angle, Φ , made by T_{Res} to the vertical is given by

$$\Phi = \tan^{-1} (T_Y / T_Z) \quad (3.1)$$

Even though counter-intuitive, previous studies on cyclorotors at MAV-scales have shown that the measured sideward force (T_Y) could be a significant fraction of the vertical force (T_Z), even as high as 55% [15]. Recent analytical studies showed that the reason for this is large flow curvature effects for cyclorotors with high chord/radius ratio and unbalanced drag forces in the upper and lower halves resulting in net sideward force [18]. A detailed explanation of the flow curvature effects was provided in section 3.2.1.

Moving to the UAV-scale, the current study found that the sideward forces persisted, but were highly dependent on the geometric parameters. This is shown in Figs. 3.2 and 3.3, where the variation of thrust components produced by a 2-bladed cyclorotor with a chord/radius ratio of 0.26 and a 6-blade cyclorotor with a chord/radius ratio of 0.66 with operating pitch amplitudes of $\pm 30^\circ$ is plotted as a function of rotational rate. The points represent experimental measurements and the dotted lines represent quadratic curve fits. Examining the 2-bladed rotor (3.2), T_Y never exceeded 12% of T_Z representing a value of 6° for ϕ or a 1° deviation from the expected when considering the mechanical phase lag of 5° resulting from the four-bar pitching mechanism. Increasing the number of blades to four shows an increase in T_Y up to 80% of T_Z (Fig. 3.3). This increase equates to an increase in ϕ up to 35° (after considering mechanical phase lag) or in other words, the resultant thrust vector (T_{Res}) will be tilted at an angle of 35° with the vertical.

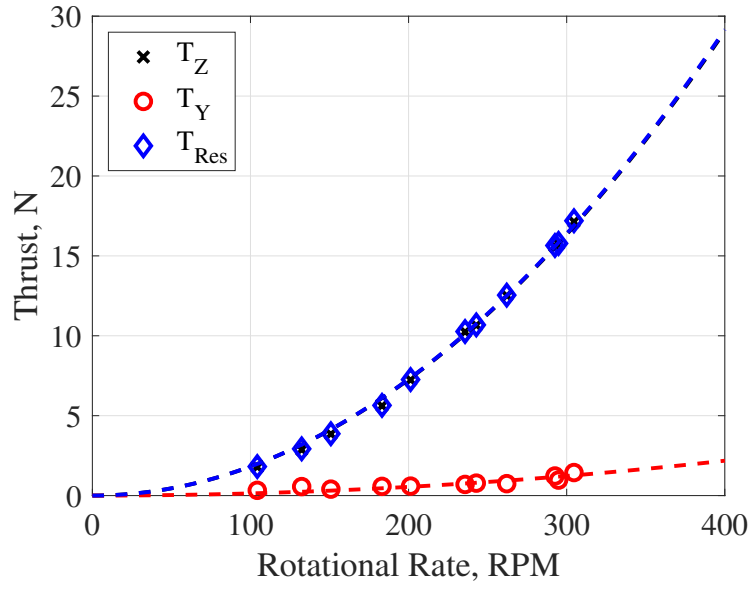


Figure 3.2: Thrust vs. RPM: 2-bladed cyclorotor. $c/R = 0.26$, $PA = \pm 30^\circ$

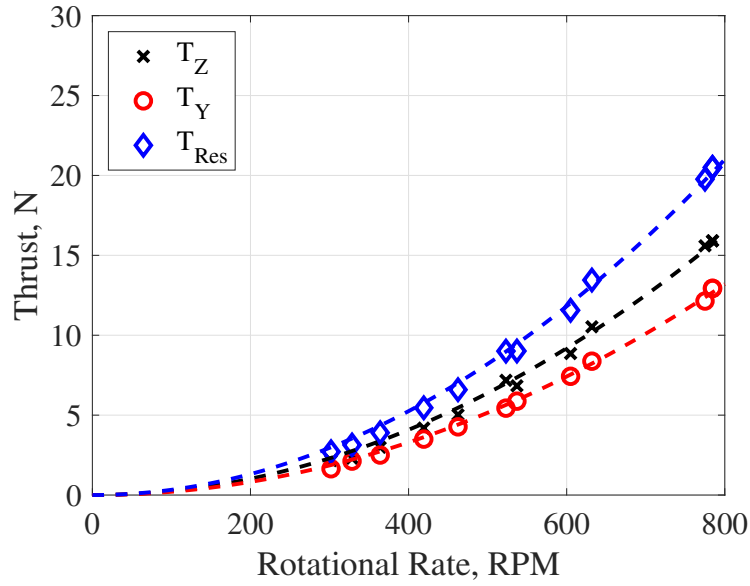


Figure 3.3: Thrust vs. RPM: 6-bladed cyclorotor. $c/R = 0.66$, $PA = \pm 30^\circ$

Adjusting the phasing of the pitch kinematics ensures the resultant thrust is directed in the desired direction thus the remainder of the study presents thrust as the resultant thrust (Eq. 3.2) unless stated.

$$T_{Res} = \sqrt{T_Y^2 + T_Z^2} \quad (3.2)$$

Referring to Figures 3.2 and 3.3, we see that, as expected, according to momentum theory, thrust increases as the square of rotational speed.

3.1.2 Power Analysis

The total aerodynamic power of a cyclorotor is a combination of the induced and profile power of the blades, blade pitching power, and the parasitic losses associated with rotating support structure. Power was obtained as the product of measured torque and rotational speed (Eq. 3.3). Tare tests with no blades mounted to the rotor were conducted at various rotational speeds to measure the parasitic power associated with the support structure. The tare power measurements were subtracted from the total aerodynamic power to obtain the power required to rotate only the blades. Tare losses accounted for less than 5-10% of the total aerodynamic power.

$$P = Q\Omega \quad (3.3)$$

The aerodynamic power measurements for the same 2- and 6-bladed cyclorotors from the previous section are provided in Figs. 3.4 and 3.5, respectively. Again, as expected according to momentum theory, power increases as the cube of rotational speed.

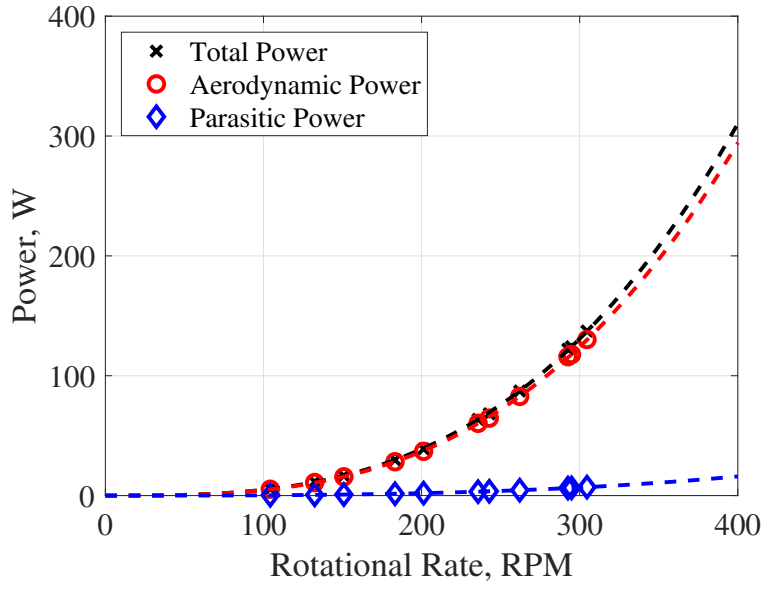


Figure 3.4: Power vs. RPM: 2-bladed cyclorotor. $c/R = 0.26$, $PA = \pm 30^\circ$

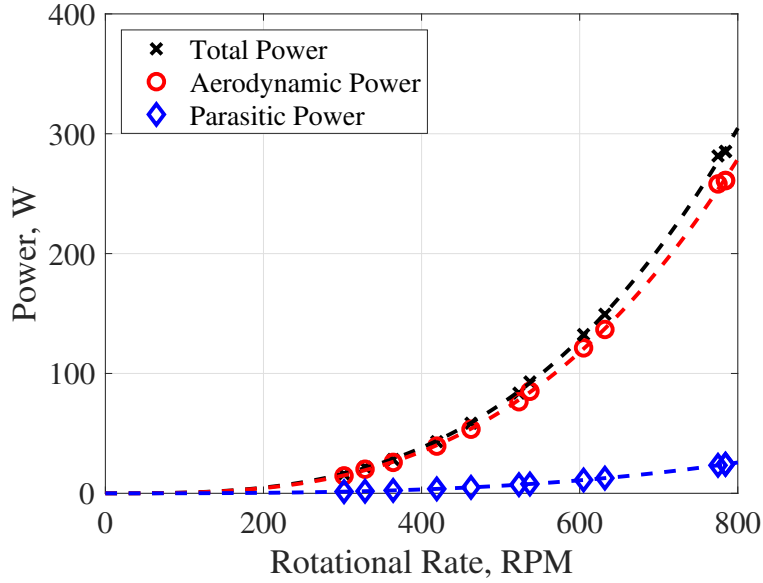


Figure 3.5: Power vs. RPM: 6-bladed cyclorotor. $c/R = 0.66$, $PA = \pm 30^\circ$

3.2 Rotor Parameters

3.2.1 Virtual Camber

The curvilinear flow experienced by the cyclorotor blades introduces a unique aerodynamic phenomenon referred to as virtual camber (Fig. 3.6). The virtual camber effect was originally

observed on vertical axis wind turbine blades where the blades undergo an orbital motion and therefore operates in a similar curvilinear flow. The effect is introduced now due to its significant effect on aerodynamic performance of a cyclorotor. Blades subjected to curvilinear flow behave very differently compared to one immersed in a rectilinear flow. In a curvilinear flow, the local velocity and angle of attack of the blade are unique at different locations along the chord. Because of this, a symmetric blade in curvilinear flow can be viewed to behave like a cambered blade in rectilinear flow (Fig. 3.6a).

The flow curvature effects are clearly explained in Fig. 3.6b, which shows a symmetric airfoil at a 0° pitch angle. Point A is the pitching axis of the blade. For the sake of explanation, resultant velocity at any location on the blade chord was assumed a function of the rotational speed only (ignoring induced velocity and pitch rate effects). Thus, the magnitude and direction of the resultant velocity varies along the chord. The angle of attack of the flow at any location on the chord, x , is given by $\alpha_x = \tan x / R^{-1}$ and the velocity magnitude is given by ΩR where $R' = \sqrt{R^2 + x^2}$. The flow curvature effects become more pronounced as the chord-by-radius ratio and pitch amplitude increase thus, the virtual camber effect is directly dependent on the cyclorotor configuration and plays a significant role in the thrust generation and aerodynamic performance

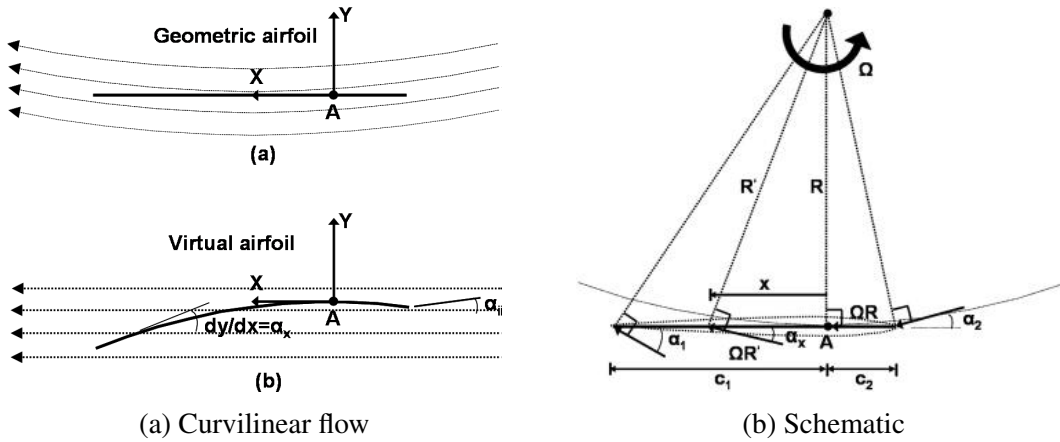


Figure 3.6: Virtual camber effect.

3.2.2 Effect of Blade Cyclic Pitching Amplitude

The cyclic blade pitching amplitude for a cyclorotor is analogous to collective pitch for a conventional rotor and it plays a significant role in the performance of the cyclorotor because the amplitude directly impacts the resultant thrust produced and aerodynamic efficiency. Operating at the optimum cyclic pitching amplitude is important to maximize the cyclorotor's thrust and power loading. Previous studies at the MAV scale have shown that operating at high cyclic pitching amplitudes ($> \pm 40^\circ$) improves the performance of the cyclorotor [31]. The reason for the improved performance at high cyclic pitch amplitudes finds its roots in the unsteady aerodynamics due to the pitch-rate and flow curvature.

Figures 3.7 and 3.8 present power loading vs disk loading for a 2- and 4-bladed cyclorotor featuring a 5.5 in chord, 22 in span, and 8.25 in radius with symmetric pitch kinematics between $\pm 15^\circ$ and $\pm 40^\circ$. Symmetric pitch kinematics means the blades attain the same cyclic pitch angle at diametrically opposite locations of its circular trajectory. Examining the results for the 2-bladed cyclorotor in Fig. 3.7 one can see the effect of cyclic blade pitching amplitude on power loading. The power loading for all disk loadings steadily increases from the $\pm 15^\circ$ pitch amplitude case all the way to the $\pm 35^\circ$ case after which point it begins to decrease. The drop-in power loading for the $\pm 40^\circ$ case is small and is likely due to the onset of dynamic stall and shows that, when considering aerodynamic efficiency, $\pm 35^\circ$ is the optimal symmetric cyclic pitch amplitude for the current 2-bladed cyclorotor. Experimental results for the 4-bladed cyclorotor shown in Fig. 3.8 demonstrate trends comparable to the 2-bladed one. The power loading for each disk loading steadily increases from the $\pm 15^\circ$ pitch amplitude case up to the $\pm 40^\circ$ pitch amplitude. The increase in optimal cyclic pitch amplitude from the 2- to 4-bladed case is attributed to the change in inflow which reduces the effective angle of attack.

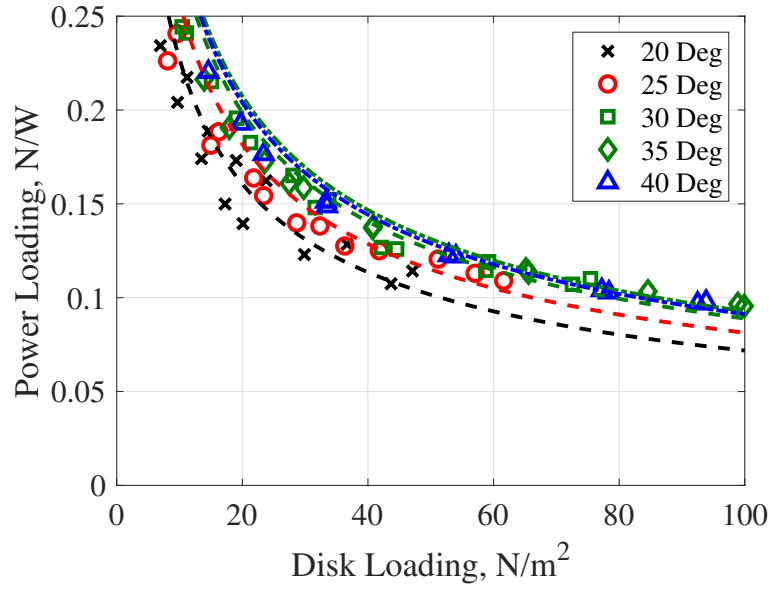


Figure 3.7: PL vs. DL : 2-bladed cyclorotor. $c/R = 0.66$, varying symmetric pitch amplitudes

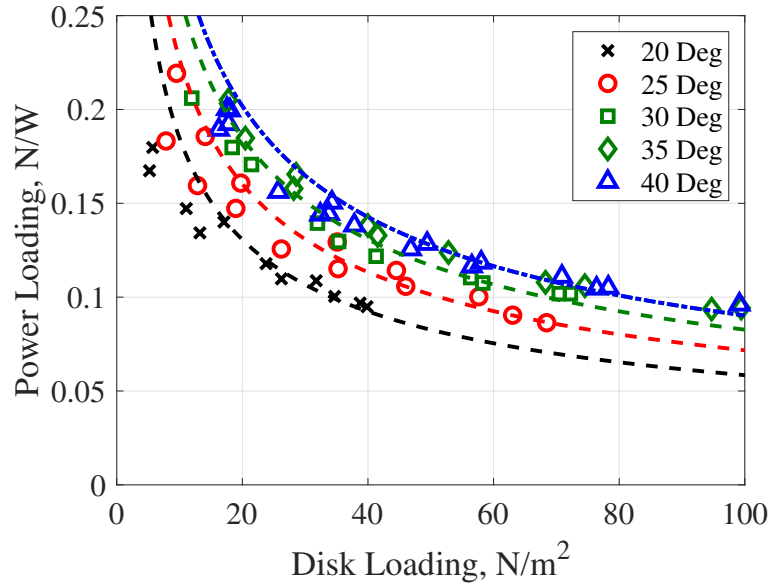


Figure 3.8: PL vs. DL : 4-bladed cyclorotor. $c/R = 0.66$, varying symmetric pitch amplitudes

Previous MAV-scale studies showed a measurable improvement in aerodynamic efficiency for asymmetric pitching kinematics [13]. The improvement was found when the pitch amplitude was higher at the top ($\psi = 90^\circ$) than the bottom ($\psi = 270^\circ$) of the trajectory and was attributed to the inflow and flow curvature effects, which reduce the lift produced along the top of the trajectory

and increases it along the bottom. To understand the effect of asymmetric pitching on a UAV-scale cyclorotors aerodynamic efficiency, Figs. 3.9 and 3.10 present power loading vs disk loading for the 2- and 4-bladed cyclorotors with five different pitch kinematics featuring an overall 70° peak-to-peak amplitude. Unlike the MAV-scale studies, a negligible or even detrimental effect was found for pitch kinematics featuring 5° or 10° of asymmetry in the pitch amplitude for both 2-bladed and 4-bladed rotors regardless of the location of the higher pitch amplitude.

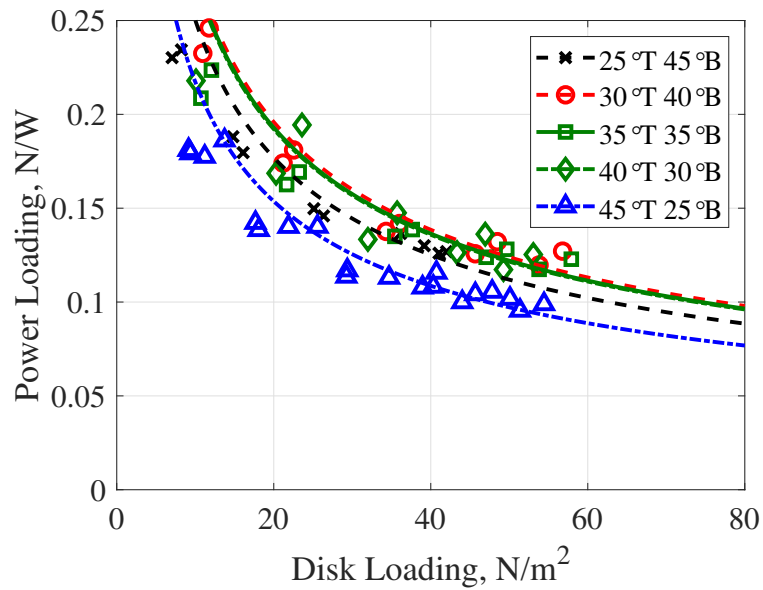


Figure 3.9: PL vs. DL: 2-bladed cyclorotor. $c/R = 0.66$, varying asymmetric pitch amplitudes

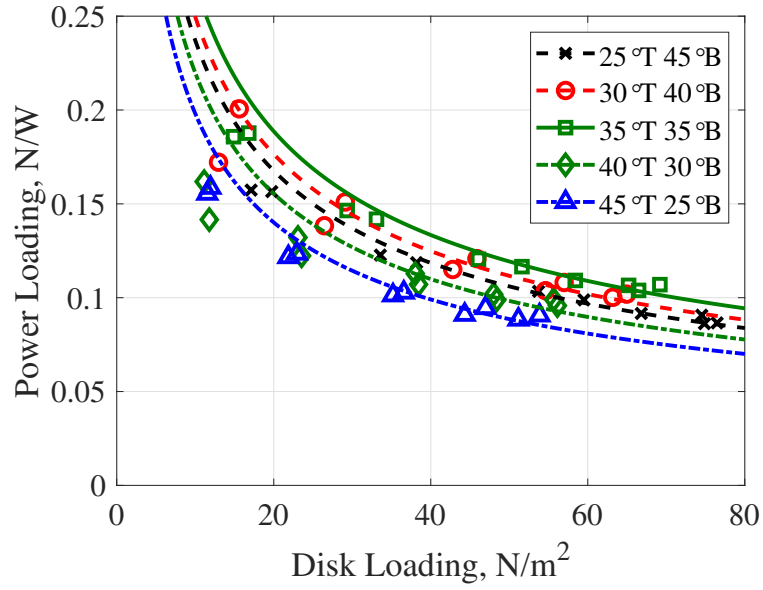


Figure 3.10: PL vs. DL: 4-bladed cyclorotor. $c/R = 0.66$, varying asymmetric pitch amplitudes

The complex nature of the unsteady aerodynamics and flow curvature effects in a cyclorotor means the optimal pitch kinematics will shift with changing rotor geometry. Figure 3.11 presents the optimal pitch amplitude vs. chord-by-radius ratios for a 2-bladed UAV-scale cyclorotor (symmetric pitching). The optimal pitch amplitude is determined based on the maximum power loading for a fixed disk loading of $60 N/m^2$. The increase in optimal pitch amplitude with increasing chord-by-radius ratio is attributed to the significant change in flow curvature effects. As discussed in section 3.2.1 an increase in chord-by-radius ratio results in an increased velocity gradient across the blade chord resulting in an increased virtual camber.

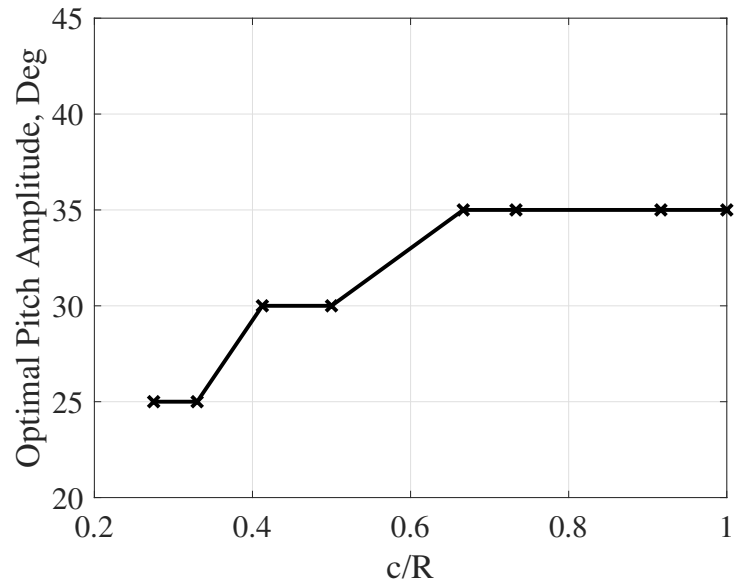


Figure 3.11: Optimal Pitch Amplitude vs. Chord-by-Radius Ratio: 2-bladed cyclorotor

Figure 3.12 presents the optimal pitch amplitude vs number of blades for fixed chord-by-radius ratios of 0.26, 0.50, and 0.66. The change in optimal pitch amplitude with increasing number of blades was less significant but is attributed to the changing inflow which leads to a reduction in the effective angle of attack. To capture the optimal pitch amplitude for each configuration the remainder of the paper presents results for symmetric pitching kinematics with a maximum cyclic pitch amplitude between $\pm 15^\circ$ and $\pm 40^\circ$.

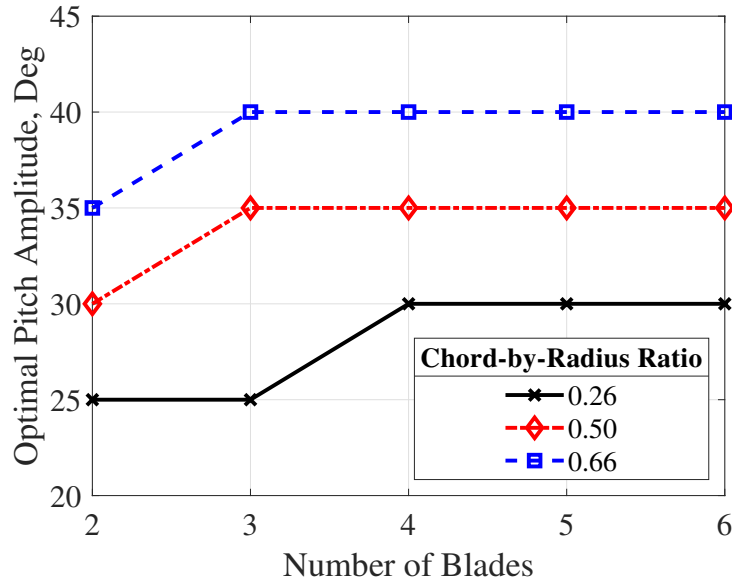


Figure 3.12: Optimal Pitch Amplitude vs. Number of Blades: varying chord-by-radius ratio

3.2.3 Effect of Blade Airfoil Thickness

The pitching kinematics for a cyclorotor result in a geometry such that the top surface of the blade relative to the incoming flow becomes the bottom surface during the opposite half of the cycle (Fig. 1.1b). Inherent from this fact is that the ideal airfoil likely has a symmetric geometry, as was found during MAV-scale studies [13]. A cambered geometry would operate with one half of the cycle experiencing a positive camber while the other would operate in negative camber. The results presented in this paper are focused on determining the ideal airfoil thickness from tests on blades with symmetric 4-series NACA airfoils with 15%, 20% and 25% thickness-to-chord ratios, namely NACA0015, NACA0020 and NACA0025 airfoils. The other parameters fixed for these tests included a 5.5 in chord, 21 in radius ($c/R=0.26$), and 22 in span.

Figure 3.13 shows the variation of thrust coefficient, C_T , with pitch amplitude (calculated at a blade speed of 20 m/s (~ 400 RPM) or a Reynolds number of $\sim 200,000$). As expected, the results for varying airfoils is subtle but the results provided are quite interesting. Looking at the values of the coefficient of thrust we see that the thrust is higher for the thinnest airfoil for most of the operating pitch amplitudes. At the higher pitch amplitudes ($\pm 35^\circ$) the thrust begins to become nonlinear, which is indicative of stall, for the blade featuring the NACA0015 airfoil. The

thicker airfoils (NACA0020 and NACA0025) exhibit a delay in the onset of this nonlinear behavior resulting in higher thrust production for the thicker airfoils at higher pitch amplitudes.

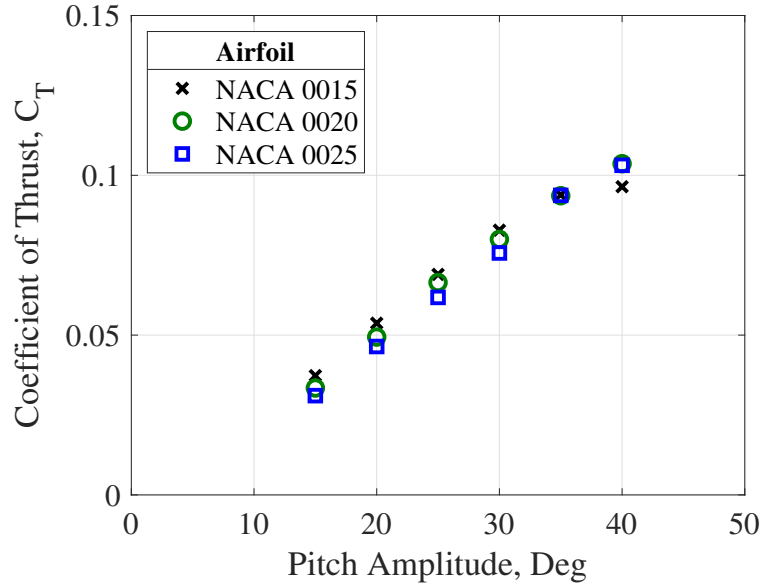


Figure 3.13: C_T vs. Pitch Amplitude: varying airfoil thickness

Figure 3.14 shows the variation of power coefficient, C_P , with pitch amplitude for the different airfoils tested. For all pitch amplitudes, the thinner airfoils exhibit increased aerodynamic power, which is counter intuitive when considering conventional propeller aerodynamics where thinner airfoils tend to exhibit reduced drag and thus reduce power requirements. The deviation is attributed to the higher stall angle of thicker airfoils and performance change associated with the virtual camber effect.

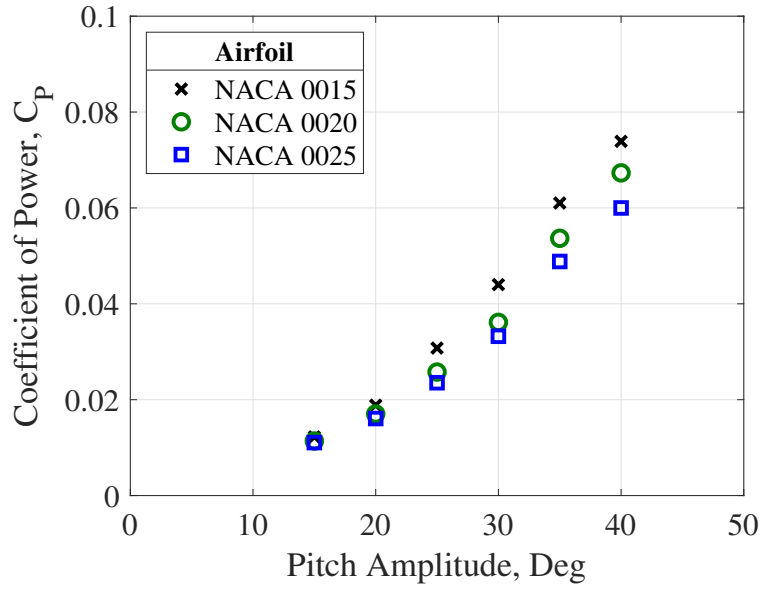


Figure 3.14: C_P vs. Pitch Amplitude: varying airfoil thickness

Combining the effects on thrust and aerodynamic power due to airfoil thickness, Fig. 3.15 shows the power loading for a fixed disk loading of 60 N/m^2 . Two interesting trends arise while examining the plots. First, note the peak power loading values are near identical ($PL \approx .165 \frac{\text{N}}{\text{W}}$) for all airfoils and it occurs at either a $\pm 20^\circ$ or $\pm 25^\circ$ pitch amplitude. Second, note the shape of the PL vs pitch amplitude plot is different from one airfoil to another. With the thinnest airfoil (NACA 0015), a sharp peak could be seen centered about a 20° pitch amplitude. Moving to the thicker airfoils (NACA 0020 and NACA 0025) the peak shifts to 25° and a more rounded peak to the power loading curve exists, which provides an expanded operating regime in which the cyclorotor can produce thrust efficiently. Based on these results, a symmetric airfoil with a thickness of around 20 to 25 percent of the chord is recommended from an aerodynamic efficiency standpoint. Improved performance at higher thickness is also an encouraging result from blade structural design standpoint. The airfoil used for the remainder of the study was a NACA 0020.

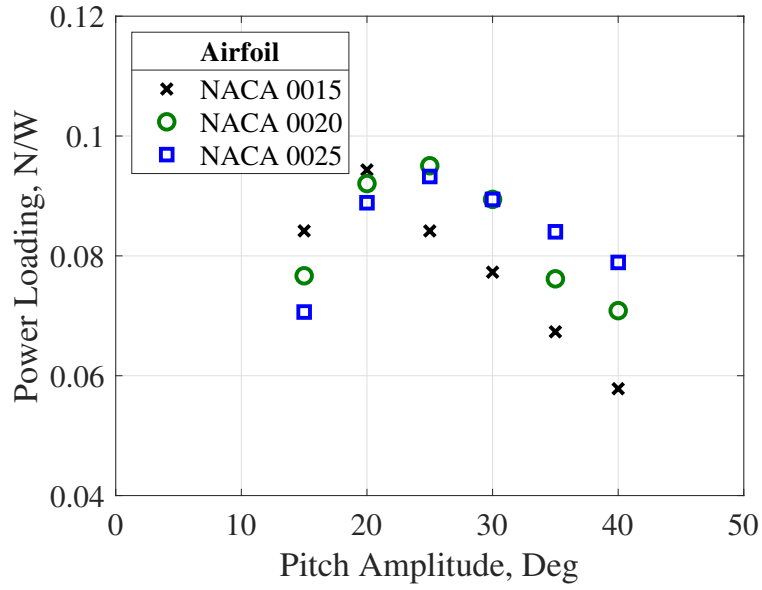


Figure 3.15: PL vs. DL : varying airfoil thickness

3.2.4 Effect of Blade Span (Blade Aspect Ratio)

2-bladed cyclorotors with three different blade spans (16.5 in., 22in., and 27.5 in.) were tested at the same chord (5.5 in.) and blade kinematics for two different radii (8.25 in. and 11 in.) to understand the effect of blade span on thrust generation and aerodynamic efficiency. The spans and chord were chosen to equate to aspect ratios of 3, 4 and 5 while the tested radii equated to chord-by-radius ratios of 0.50 and 0.66. The aspect ratios test were limited to a maximum of 5 to mitigate the effect of blade deflection on the results [15]. These chord-by-radius ratios were chosen due to their proximity to the optimal chord-by-radius ratio as is covered in the subsequent sections. The data points were calculated for a fixed blade speed of 20 m/s.

Figures 3.16 and 3.17 show the variation of cyclorotors thrust produced per unit span, presented as C_T/σ , and power required per unit span, presented as C_P/σ , of the cyclorotor with respect to aspect ratio. Figure 3.18 presents the power loading for a fixed disk loading (60 N/m^2). The plots include data for the two chord-by-radius ratios tested and three separate pitching amplitudes ($\pm 20^\circ$, $\pm 30^\circ$, $\pm 40^\circ$). The trends for all three figures show limited change with respect to aspect ratio. The result is significant because traditionally increasing the blade aspect ratio results in an increased aerodynamic efficiency due to reduction in tip losses.

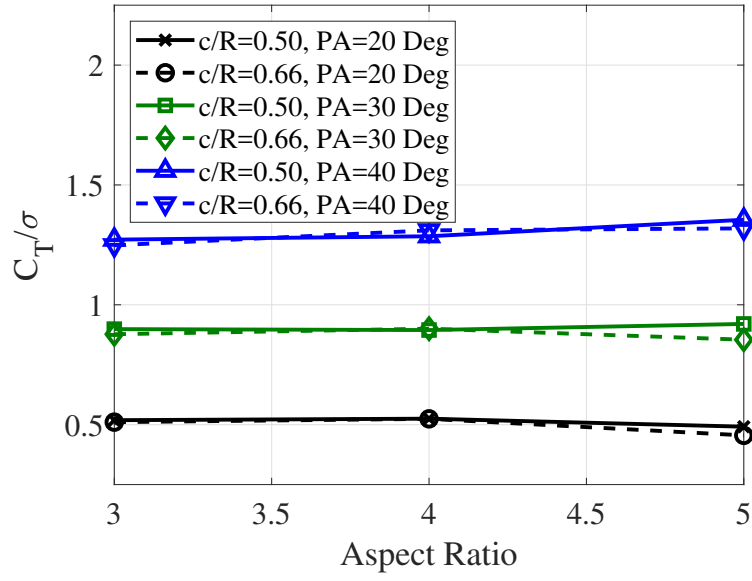


Figure 3.16: C_T/σ vs. AR : varying chord-by-radius and pitch amplitude

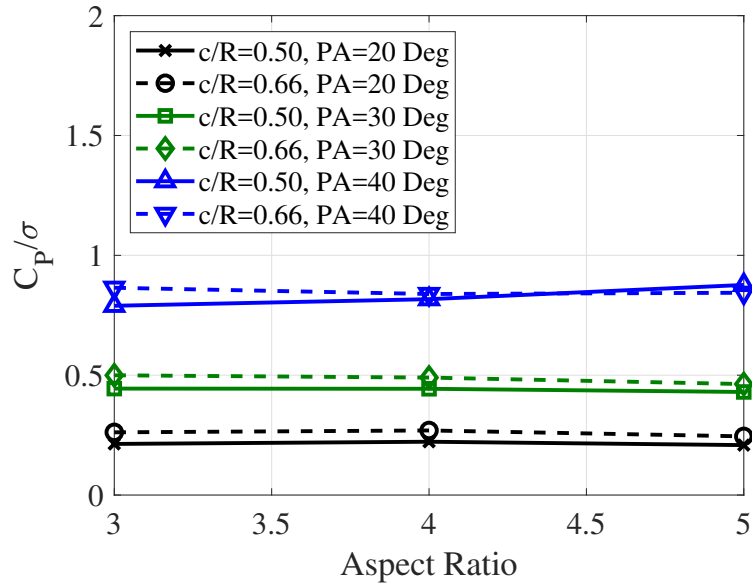


Figure 3.17: C_P/σ vs. AR : varying chord-by-radius and pitch amplitude

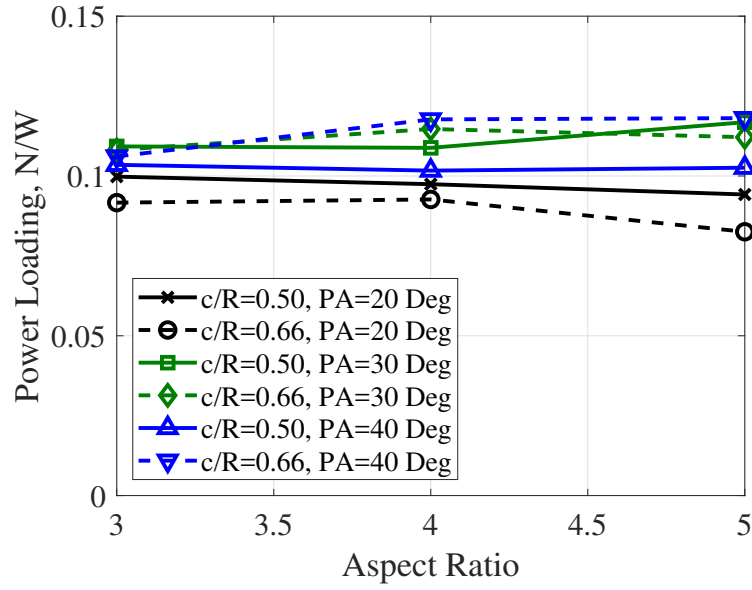


Figure 3.18: PL vs. AR for fixed disk loading: varying chord-by-radius and pitch amplitude

To investigate the magnitude of the tip losses an experiment was conducted using a 2-bladed cyclorotor with an aspect ratio of 4 to examine the relative change in thrust generation and aerodynamic efficiency for rotors with and without end plates. For the experiment a thin elliptical plate was attached to the end of each blade (Fig. 3.19). Figure 3.20 shows the power loading vs. disk loading for the optimal pitch amplitude for that configuration (25°). The dotted lines represent a curve fit based on a quadratic fit for thrust and cubic fit for power with respect to rotational rate. The results demonstrate a small, but noticeable ($\sim 2\%$) change in the power loading. The small change for This result provides confidence in the assertion above that thrust generation and aerodynamic efficiency exhibit minimal changes with regards to blade aspect ratio for the small aspect ratios typically associated with cyclorotors. Large aspect ratios ($AR > 5$) could result in improvements in aerodynamic performance, but special consideration must be made with regards to the structural design of high aspect ratio blades.



Figure 3.19: 2-bladed cyclorotor with elliptical endplate

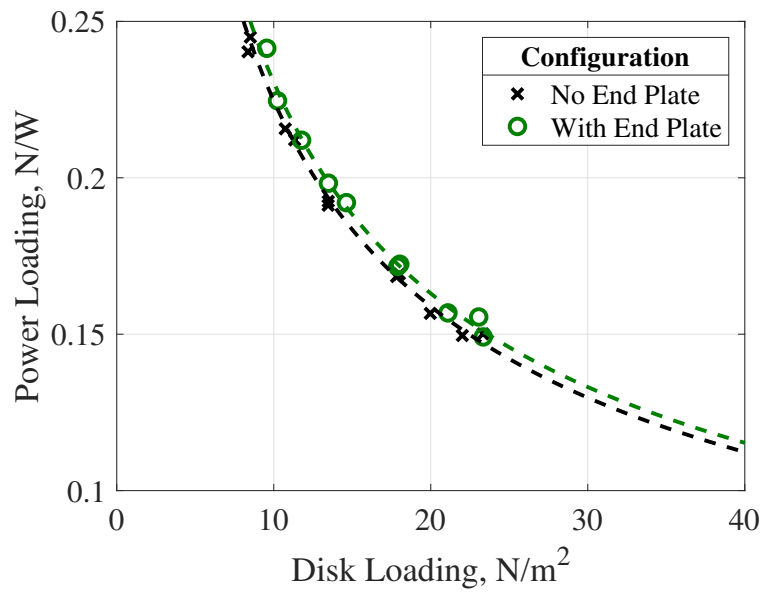


Figure 3.20: PL vs. DL : 2-bladed cyclorotor with and without endplate

3.2.5 Effect of Chord-by-Radius Ratio

The chord-by-radius ratio was proven to be one of the driving design parameters for MAV-scale cyclorotors when it comes to establishing an optimal rotor geometry [13]. The importance of the parameter is derived from the implication of chord-by-radius ratio on flow curvature effects as described in section 3.2.1.

One immediate impact of the flow curvatures is the shift in relative magnitudes of the horizontal and vertical thrust generation. Figure 3.21 presents the angle of the resultant thrust vector from vertical, Φ (Fig. 2.1), versus the chord by radius ratio. Specifically, these tests were conducted on a cyclorotor with a 5.5 in chord and 22 in span at a fixed blade speed of 20 m/s for radii between 5.5 in. and 21 in. In Figs. 3.21 to 3.24 the chord-by-radius ratio is increased by decreasing the radius for a fixed chord. The relative change in magnitude is due in part to the virtual camber effect which results in asymmetry in lift and drag coefficients between the upper and lower halves of the circular blade trajectory [32, 33]. This is because, the blade experiences negative virtual camber in the upper half of the trajectory ($\psi = 0^\circ\text{-}180^\circ$) and positive virtual camber in the lower half ($\psi = 180^\circ\text{-}360^\circ$). The positive virtual camber at the 90° azimuthal location serves to minimize the lift in the upper half while the negative virtual camber at the 270° azimuthal location amplifies the effects of curvilinear geometry leading to significant lift in the lower half. The virtual camber can also create an asymmetry between the right ($\psi = 270^\circ\text{-}90^\circ$) and left halves ($\psi = 90^\circ\text{-}270^\circ$) of the circular trajectory, leading to the forces in Y-direction not getting cancelled out. The magnitude of the virtual camber depends on the chord-by-radius ratio and hence this parameter has a profound effect on blade forces and cyclorotor performance. A cyclorotor by design is capable vectoring its thrust around the azimuth (360°), thus only the magnitude of the resultant thrust is considered going forward.

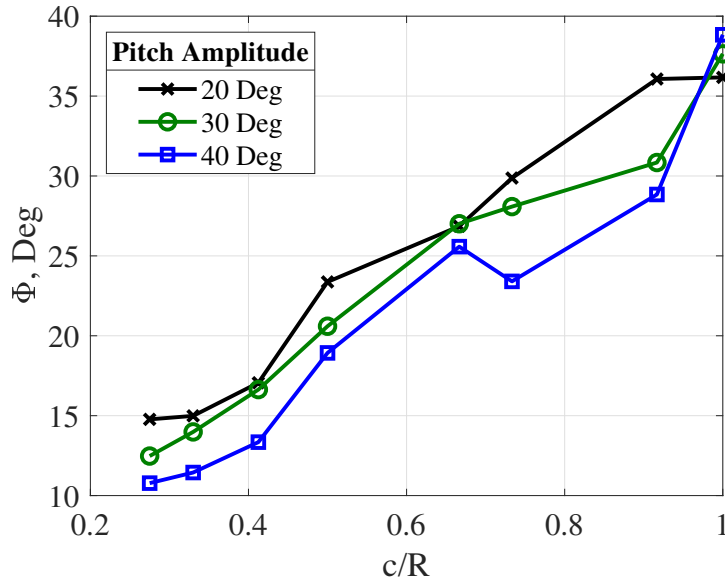


Figure 3.21: Φ vs. c/R : varying pitch amplitude

Figures 3.22 and 3.23 present thrust and power vs. chord-by-radius ratio for the same conditions defined above to examine the effect of chord-by-radius on thrust and aerodynamic power. From Fig. 3.22 it can be seen that for high pitch amplitudes that thrust is not constant for different radii at a fixed blade speed (ΩR) and chord. This is due to the change in flow curvature effects associated with the increased chord-by-radius ratio. For the case presented it was found that for high pitch amplitudes (40°), where the flow curvature effects are the highest, increasing the chord by radius ratio up to 0.66 resulted in increased thrust generation ($\sim 11\%$) using the exact same blade and blade speed. The decline in thrust generation per unit area for chord-by-radius ratios greater than 0.66 demonstrates the optimal chord-by-radius ratio in terms of thrust production lies between 0.5 and 0.66. The implication is decisive for the design of an optimal cyclorotor because by decreasing the radii you are effectively reducing rotor weight due to shorter support arms while at the same time increasing the thrust generated. The result is a cyclorotor with higher thrust generation and higher thrust to weight ratios. Looking at Fig. 3.23, it can be seen that the power increases with respect to chord-by-radius ratio for all pitch amplitudes. While still not fully understood, the change in thrust and power with changing chord-by-radius ratio are attributed to the virtual camber effects, which have an impact on the blade dynamic lift and drag as it goes

around the azimuth. As shown, these effects are beneficial to an extent but become detrimental to thrust generation and performance at very high chord-by-radius ratios ($c/R > 0.66$).

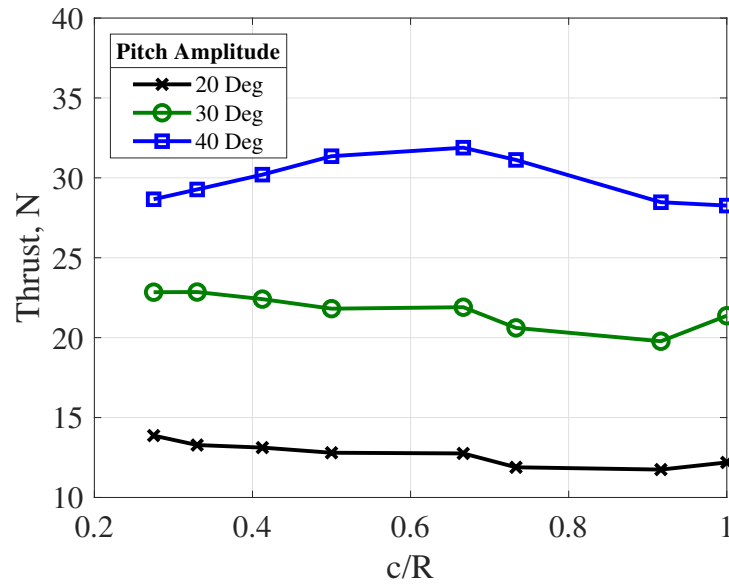


Figure 3.22: Thrust vs. c/R : varying pitch amplitude

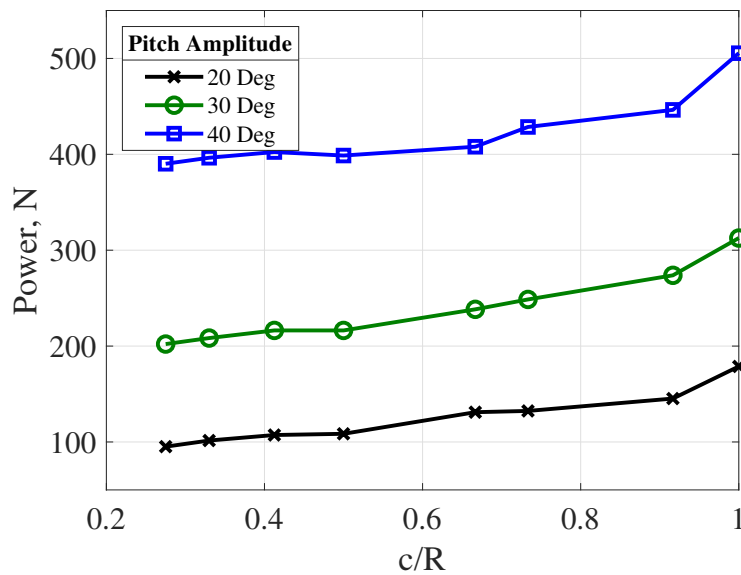


Figure 3.23: Power vs. c/R : varying pitch amplitude

Increasing the chord by radius ratio represents one of two ways to increase the cyclorotor solidity. The solidity is also dependent on the number of blades ($N_b c / 2\pi R$). Despite the large

change in solidity during the current study, the trends found for the change in thrust and power with respect to chord-by-radius are independent of the variance in solidity due to the constant blade area ($N_b bc$) and fixed blade speed (ΩR). In other words, as shown in Eq. 3.4, C_T/σ is proportional to total thrust (T_{Res}) since the total blade area and blade speeds are constant.

$$C_T/\sigma = \frac{T_{Res}}{A(\Omega R)^2} \bigg/ \frac{N_b c}{2\pi R} = \frac{\pi T_{Res}}{\rho(\Omega R)^2 N_b bc} \quad (3.4)$$

Figure 3.24 presents power loading versus chord-by-radius ratio for a fixed disk loading (60 N/m^2) to examine the effect of chord-by-radius ratio on aerodynamic efficiency. Like trends found for thrust and power, the aerodynamic efficiency varies greatly for different pitch amplitudes. For a pitch amplitude of 20° the power loading remains relatively constant until high chord-by-radius ratios, whereas for higher pitch amplitudes (30° and 40°) an optimal configuration becomes clear with the formation of a peak. In terms of aerodynamic efficiency, the optimal chord-by-radius ratio was found to be 0.66. Thus, combining considerations for the thrust generation and aerodynamic efficiency the recommend chord-by-radius ratio is around 0.66. It is significant to note while the relative change in cyclorotor performance with respect to chord-by-radius ratio was significantly different, the optimal chord-by-radius ratio was found to be similar even at an order of magnitude higher Reynolds number when compared to earlier MAV scale studies [13].

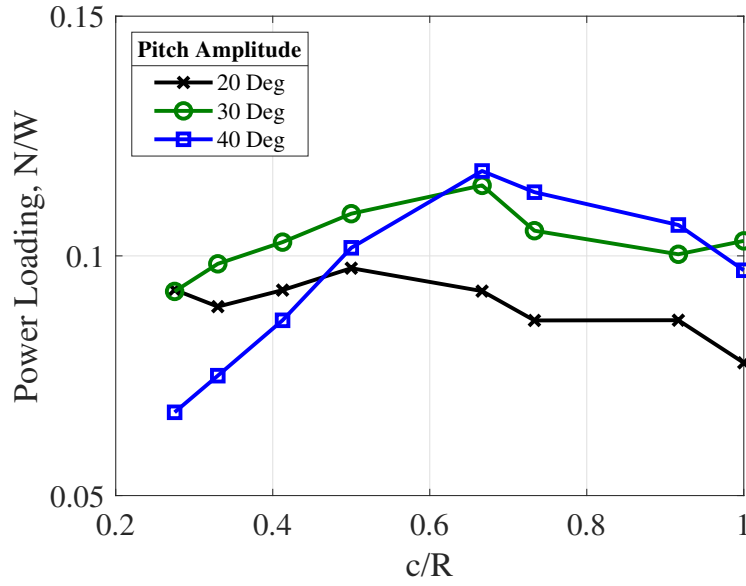


Figure 3.24: PL vs. c/R : varying pitch amplitude

3.2.6 Effect of Number of Blades

As mentioned before, increasing the number of blades serves is an alternative method to increase rotor solidity without changing the chord-by-radius ratio and flow curvature effects. To determine whether a change in number of blades has an effect independent of the change in solidity the relationship of C_T/σ , C_P/σ , and power loading with regards to the number of blades was investigated. The studies were conducted for a single chord (5.5 in.) for three different radii (21 in., 11 in., and 8.25 in.) establishing three different chord-by-radius ratios (0.26, 0.50 and 0.66). The large variance creates significant difference in the flow curvature effects on the rotor performance allowing for its effects to be neglected.

Figure 3.25 presents C_T/σ vs number of blades for the rotor configurations operating at a fixed blade speed (20 m/s) for three separate pitch amplitudes (20°, 30°, and 40°). Examining the figure, one can observe that C_T/σ monotonically drops with increasing number of blades. In fact, for all nine of the configurations presented, the value of C_T/σ for a 6-bladed rotor is 40-60% of that found for the 2-bladed rotor. The underlying cause of this observation is two-fold. First, the increase in the number of blades results in a shift in the inflow reducing the effective angle of attack of the blade resulting in less lift. Second, as the number of blades increases the blade interactions increase

resulting in reduced thrust generation.

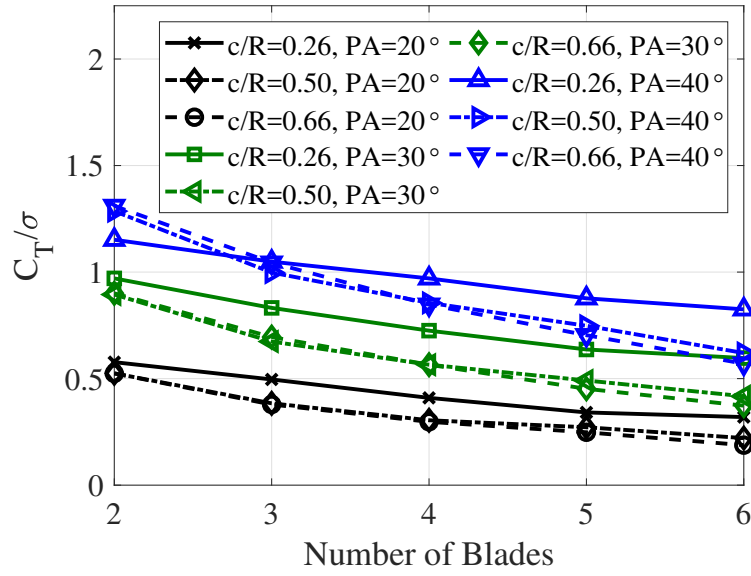


Figure 3.25: C_T/σ vs. Nb for fixed disk loading: varying chord-by-radius ratio and pitch amplitude

Transitioning to the effect of the number of blades on aerodynamic power, Fig. 3.26 shows C_P/σ versus number of blades. Similar to Fig. 3.25, C_P/σ decreases with increasing number of blades. Neither thrust nor power doubles when the number of blades is doubled.

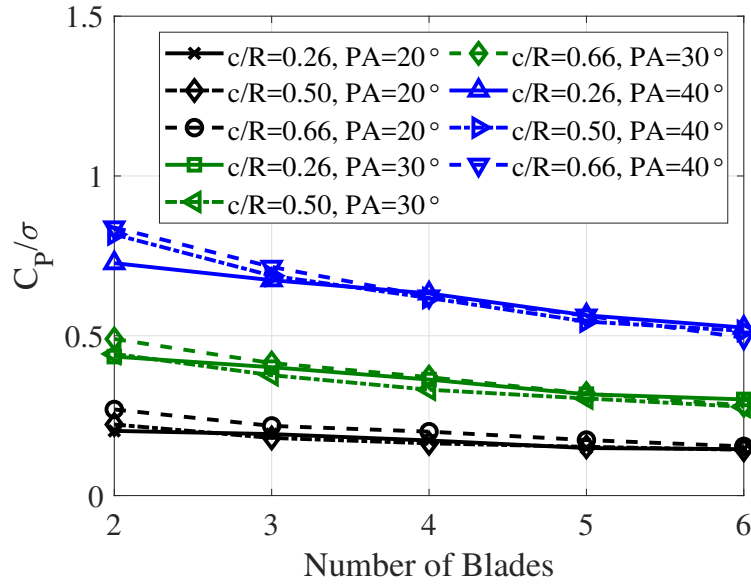


Figure 3.26: C_P/σ vs. Nb for fixed disk loading: varying chord-by-radius ratio and pitch amplitude

To determine if a trend exists for aerodynamic efficiency with regards to number of blades, the power loading was plotted versus number of blades for a fixed disk loading of 60 N/m^2 (Fig. 3.27). The trend was sporadic with regards to number of blades. The data points for the lower chord-by-radius ratio ($c/R = 0.26$) exhibited an increase in power loading for all number of blades. The larger chord-by-radius ratio ($c/R = 0.50$ and 0.66) exhibited an overall decreasing trend with regards to power loading. To design an aerodynamically optimal cyclorotor, there must be a balance between the chord-by-radius ratio and number of blades. This balance is likely related to the blade interactions which would be closely associated with rotor solidity and is investigated in section 3.2.7.

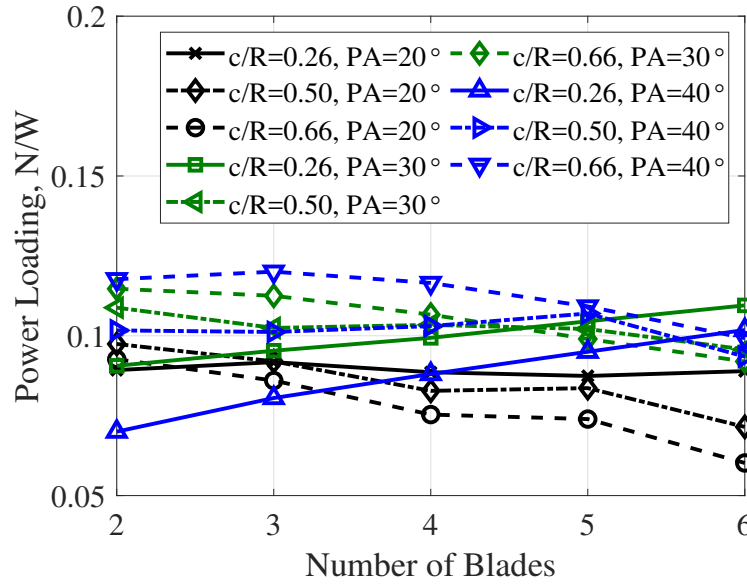


Figure 3.27: PL vs. Nb for fixed disk loading: varying chord-by-radius ratio and pitch amplitude

3.2.7 Effect of Rotor Solidity

Two ways of increasing the solidity of a cyclorotor, essentially, increasing the chord-by-radius ratio or increasing the number of blades, were investigated in the sections 3.2.5 and 3.2.6. Increasing the chord-by-radius ratio was shown to result in an increase in C_T/σ and power loading for chord-by-radius ratios up to 0.66. Increasing the number of blades was shown to result in a decrease of C_T/σ while having varied effect on the aerodynamic efficiency depending on the rotor configuration. Between the two studies it has become evident that determining the optimal configuration in terms of aerodynamic efficiency requires a balance between the chord-by-radius and number of blades.

Figure 3.28 presents C_T/σ vs. solidity for rotors operating at a $\pm 40^\circ$ pitch amplitude with varying rotor solidity based on the two different methods. Based on the trends it becomes clear that to improve thrust per unit area a designer should choose the optimal chord-by-radius because increasing the number blades results in steep penalties in terms of thrust per unit area. However, increasing the chord-by-radius ratio can result in double the thrust for double the blade area.

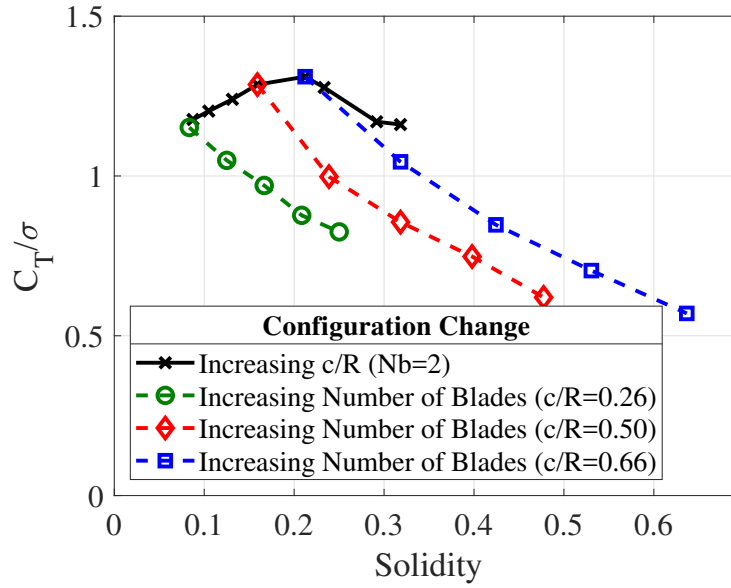


Figure 3.28: C_T/σ vs. σ : varying rotor configuration

This possibility was further investigated by conducting experiments with blades of three different chord lengths ($c=5.5$ in, 8 in, and 10 in.) at a fixed radius ($R = 13.33$ in.) equating to chord-by-radius ratios of 0.41, 0.60 and 0.75. Figure 3.29 presents C_T/σ vs. solidity from those experiments. For pitch amplitudes of 20° and 30° , the thrust per unit area remained roughly constant while for 40° a slight decrease was found. The results correlated well with the study on changing chord-by-radius ratio for a fixed chord discussed previously thus doubling the blade area by changing the chord length can result in double the thrust assuming the optimal chord-by-radius ratio (~ 0.66) is not exceeded. The reduction in the total number of blades also reduces the total rotor weight due to a reduction in the number of support arms and pitch links required. Due to large centrifugal loads, the support arms tend to represent a significant percentage of the rotors weight.

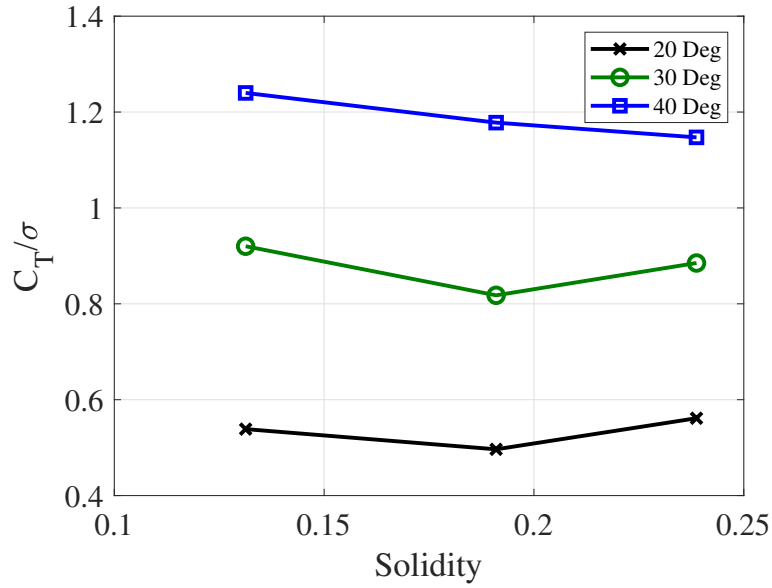


Figure 3.29: C_T/σ vs. σ : varying rotor configuration

Figure 3.30 presents power loading vs. solidity for all configurations tested as part of the number of blades and chord-by-radius ratio study for a $\pm 40^\circ$ pitch amplitude. Examining the figure, a trend begins to take shape as to the relation between figure of merit and solidity. The curve for increasing number of blades at a low chord by radius ratio ($c/R=0.26$) showed the power loading continued to increase for all values of solidity. The curve for increasing chord-by-radius ratio for a 2-bladed rotor showed a peak transition point equating to the determined optimal chord-by-radius ratio ($c/R=0.66$, $\sigma=0.24$). The final curve started with the optimal chord-by-radius ratio and presented the effect of increasing number of blades. For this curve, the power loading remained roughly constant until a solidity of ~ 0.35 , after which it began to decrease. At higher solidities, it is likely, as discussed earlier, that blade interactions begin to become detrimental to the aerodynamic performance. The optimal rotor solidity was found to fall between 0.30 and 0.40.

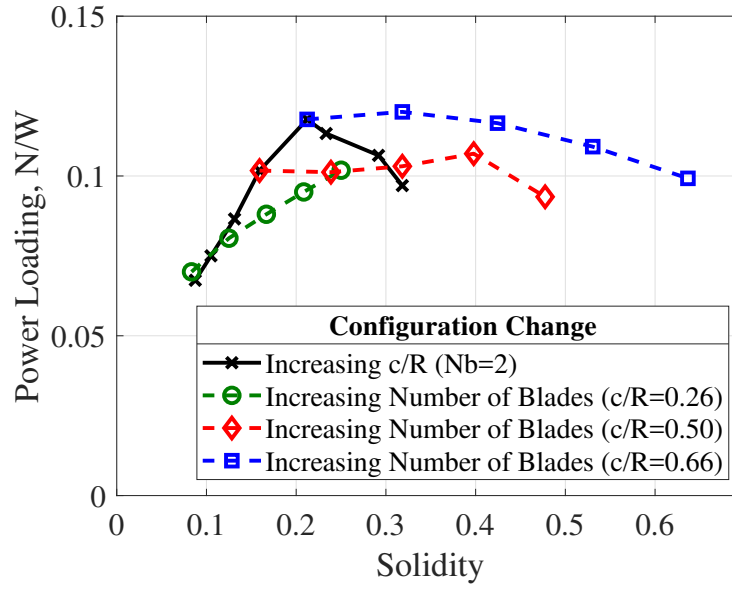


Figure 3.30: PL vs. σ : varying rotor configuration

3.3 Optimal Geometry

As a final check to determine if there was a rotor configuration tested to date that demonstrated a higher aerodynamic efficiency, the peak figure of merit obtained for all 37 rotor configuration (regardless of pitch amplitude) was plotted versus rotor solidity in Fig. 3.31. Figure of merit ($T_{Res}^{3/2}/P\sqrt{2\rho A}$) represents the ratio of ideal aerodynamic power to measured aerodynamic power. Examining the figure, the peak figure of merit was found to be 0.6. The respective rotor configuration was a 3-bladed cyclorotor with a 5.5in chord, 22in. span, and 8.25 in radius. In general terms, the recommended rotor configuration for an aerodynamically optimized UAV-scale cyclorotor is a 3-bladed rotor with a chord-by-radius ratio of 0.66, a blade aspect ratio (span/chord) of 4, a NACA 0020 airfoil, a rotor aspect ratio (span/diameter) of 1.33 and operating pitch amplitude of $\pm 40^\circ$. A picture of the optimal cyclorotor is provided in Fig. 3.32.

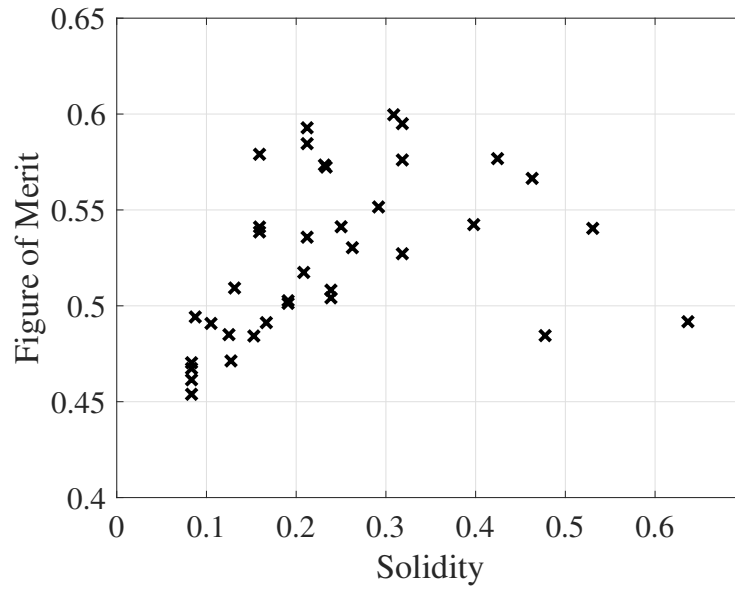


Figure 3.31: PL vs. σ : optimal pitch kinematics for every rotor configuration



Figure 3.32: Optimal cyclorotor configuration

3.4 Concluding Remarks

This present chapter discussed a detailed experimental study to understand the effect of blade kinematics and rotor geometry on the aerodynamic performance of a UAV-scale cyclorotor in hover. The study was accomplished through the development and use of a custom three-component

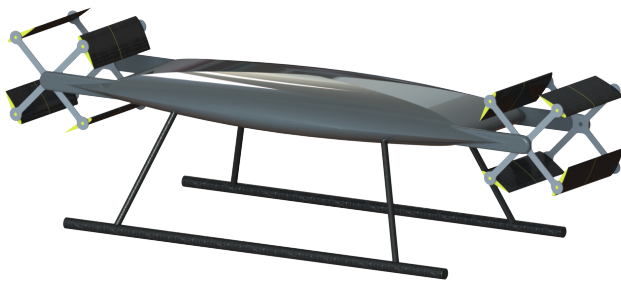
balance to measure time-averaged forces, torque and rotational speed of a UAV-scale cyclorotor prototype. Closely examining the thrust, power, and power loading measurements at different pitch amplitudes (symmetric and asymmetric), blade airfoil thicknesses, blade spans, chord-by-radius ratios, blades numbers, and solidities provides guidance on the design of an optimized cyclorotor.

4. TECHNOLOGY DEMONSTRATOR PROTOTYPE

In order to demonstrate the utility and function of a UAV-scale cyclorotor a 17 lb technology demonstrator prototype was developed with a novel dual-cyclorotor configuration [34]. Prior dual-cyclorotor configurations have featured a side-by-side arrangement of cyclorotors with a conventional tail rotor to counteract the primary cyclorotors' torque and produce excess lift. The cyclocopter developed as part of the current study features two cyclorotors with one positioned at the front and one at the rear of the vehicle. In order to achieve stable hovering flight, the vehicles cyclorotors feature a novel split-blade design. The current chapter discusses the design and development of the vehicle, the formulation and implementation of the control strategy for hover, and the flight testing results.

4.1 Vehicle Design

The current vehicle is designed to demonstrate and take full advantage of a cyclorotors thrust vectoring and high-speed flight capability. The concept features two cyclorotors on the front and rear of the vehicles fuselage (Fig. 4.1a). To maintain VTOL capabilities, the cyclorotors must be capable of producing differential forces capable of providing roll and yaw control authority. To generate these forces the cyclorotors feature a novel split-blade design, where the blade is split at mid-span location into left and right halves as shown in Fig. 4.1b. The split-blade design allows independent pitch amplitude and phase control for each half enabling different thrust magnitude and direction for the left and right sides of a single cyclorotor for roll and yaw control. Pitch control could be achieved by a differential pitch amplitude or rotational speed between front and rear rotors.



(a) Rendering



(b) Split blade design

Figure 4.1: Cyclocopter concept

The cyclocopter developed for the current study is shown in Fig. 4.2. The vehicle measures approximately 2 feet in width, 5 feet in length, and 2.5 feet in height. The gross weight of the vehicle with batteries is 17 lb. The fuselage of the vehicle was created using a system of 1/2" composite tubes and 3D printed joints to create a lightweight and stiff frame for the cyclorotors. A central composite plate provides a mounting place for the vehicles electronics and potential payloads. The cyclorotors have an 18-inch diameter, 18 in span, and 6 in blade chord. The rotors are independently driven by a 105 kV out-runner KDE motor via a single stage timing belt transmission. The nominal operating rotor rotational speed is 850 RPM.



Figure 4.2: 17 lb cyclocopter pictured with 29 g cyclocopter

Pitch amplitude and phase (analogous to collective and cyclic) control is achieved via a four-bar pitch mechanism controlled by a linear servo and rotational servo. Power is provided by two 25S 6S LIPO 6000 mAh batteries connected in series to create a 12S battery. The separate batteries allows the weight to be distributed across the vehicle. Attitude stabilization is achieved using an ultralight inertial navigation system developed at the University of Maryland, ELKA-R [35]. A summary of the design specifications is provided in Table 4.1 and a weight breakdown is provided in Table 4.2. The detailed design of the cyclorotor and its subassemblies is provided in the subsequent section.

Design Feature	UAV-Scale Cyclocopter
Cyclorotor diameter	18 inches
Blade span	18 inches
Blade chord	6 inches
Blade airfoil section	NACA 0020
Cyclic pitch amplitude	$\pm 35^\circ$
Electric motor	KDE10218XF-105
Transmission method	Timing Belt
Transmission ratio	4.17:1
Collective linear servo	Actuonix L12
Cyclic rotation servo	Turnigy TGY-6109MD
Autopilot	ELKA-R
Battery	2x 25c 6S 6000 mAh

Table 4.1: Design specifications for cyclocopter.

Component	Weight (lb)	Total (%)
Fuselage	5.50	32.4
Cyclorotors (combined)	3.50	20.6
Pitch mechanism & servos	1.85	10.9
Motors & ESCs	2.65	15.6
Batteries	3.40	20.0
Wiring & Misc.	0.10	0.5
Total	17	100

Table 4.2: Weight breakdown for cyclocopter.

4.1.1 Rotor Design

Like most VTOL aircraft, the design and development of the rotor system is the most crucial step in the vehicle design process. The present cyclorotor was designed based on the lessons learned from the experimental parametric study on hover performance presented in Chapter 3.

The design of the cyclorotor can be broken into (1) obtaining optimal rotor geometry and blade kinematics, (2) pitch mechanism design, (3) blade structural design, and (4) the design of the remainder of the rotor structure and transmission.

4.1.1.1 Rotor Geometry and Blade Kinematics

During the parametric study a number of design guidelines were formulated for use in the design of an aerodynamically optimal cyclorotor (Chapter 3). The three most important parameters were found to be the chord-by-radius ratio, number of blades, and blade pitch kinematics.

The importance of the chord-by-radius ratio is derived from the implication of the chord-by-radius ratio on flow curvature effects. The flow curvature effects are a result of the velocity distribution across the blade chord which results in a symmetric airfoil in curvilinear flow being aerodynamically similar to a cambered airfoil in rectilinear flow, referred to as virtual camber (explained in detail in section 3.2.1). The effect becomes more substantial as the chord-by-radius ratio is increased due to the increase in the velocity variation along the chord. Based on the experimental results presented previously (Section 3.2.5), the optimal chord-by-radius ratio for a cyclorotor in terms of both thrust generation and aerodynamic efficiency was found to be 0.66.

The importance of the number of blades was found to be more closely tied to the cyclorotor's solidity. The results presented as part of the study on the effect of rotor solidity (Section 3.2.7) demonstrated maximizing rotor thrust per blade area and aerodynamic efficiency requires selecting an optimized chord-by-radius ratio (0.66) and increasing the number of blades from there. Based on the experimental results, an optimal cyclorotor configuration was found to be a three bladed cyclorotor with a chord-by-radius ratio of 0.66.

Designing the cyclorotor with the proper blade pitching kinematics is equally important as

choosing the proper rotor geometry. As part of the previously presented experimental parametric study the performance of symmetric and asymmetric pitching was examined (Section 3.2.2). Results from the study showed that the optimal pitch kinematics varied significantly with the rotor geometry. Based on the experimental study the optimal pitch kinematics for a cyclorotor with four blades and a chord-by-radius ratio of 0.66 was found to be a symmetric sinusoidal motion with a maximum cyclic pitch amplitude of $\pm 40^\circ$.

Additional conclusions from the experimental study included the determination that the blade aspect ratio resulted in minimal change in cyclorotor performance for small aspect ratios and the optimal symmetric blade thickness was found to be 20% of chord (NACA 0020).

Transitioning to the vehicle rotor design, the first step was defining the desired rotor size. Considering the targeted vehicle weight of around 20 lb and previous experimental studies, the rotor diameter was chosen to be 18 inches. Based on this diameter and the optimal chord-by-radius ratio of 0.66, the blade chord was defined to be 6 inches. The rotor span was chosen to be 18 inches due to the limited effect aspect ratio has on performance and the desire for a compact vehicle width and minimized rotor weight. The rotor was designed with four rotor blades utilizing NACA 0020 airfoils as opposed to the slightly more aerodynamically efficient three blade design. The reason for this was to reduced fixed frame vibratory loads as well as increase the maximum thrust and stall margin. The cyclorotor was designed to operate with a nominal cyclic pitch amplitude of $\pm 35^\circ$ to provide a stall margin necessary for pitch and roll stability.

The final constructed cyclorotor's performance was examined in the hover stand. The measurements for thrust and power versus rotational rate are presented in Fig. 4.3. Based on the results and the final vehicle weight of 17 lb, equating to 8.5 lb of thrust required per rotor, the nominal operating RPM was found to be 850 RPM. This equated to an aerodynamic power requirement of 600 W (0.81 hp). The final rotors figure of merit was 0.58 showing a minimal decrease in efficiency with the use of a split-blade design as opposed to the solid blades tested in the experimental study.

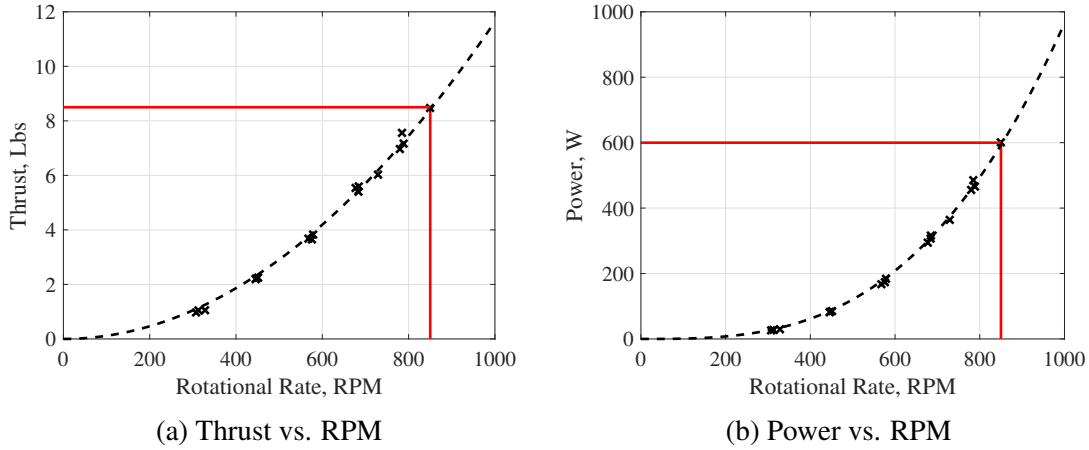


Figure 4.3: Vehicle cyclorotor performance.

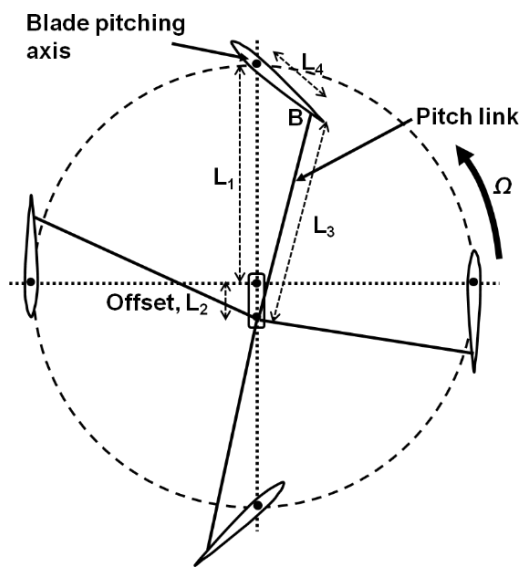
4.1.1.2 Pitch Mechanism

The pitch control mechanism developed for use on the cyclocopter must be capable of reproducing the desired pitch kinematics while also providing a means for actively controlling both the phase and pitch amplitude. The pitch mechanism design was created using a four-bar linkage (Fig. 4.4a). The radius or the rotor serves as linkage length L_1 . An offset link serves as the primary control link (L_2). L_3 is the length of the pitch link and transfers the necessary loads to achieve cyclic pitching. The distance between the connection point on the blades and the support arms serves as L_4 .

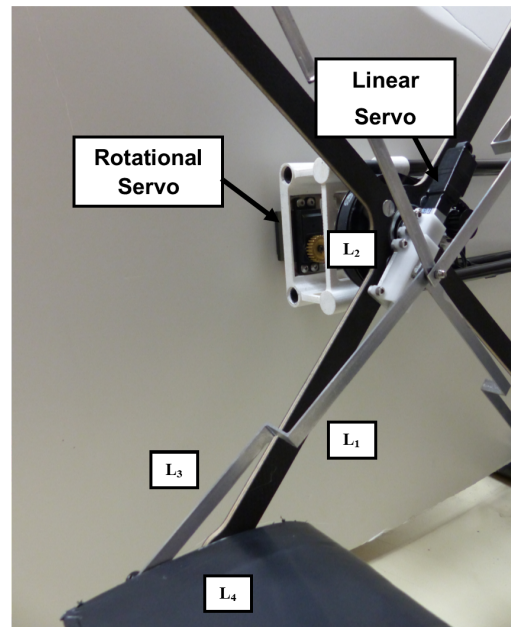
The mechanism implemented on the cyclocopter was designed to be strong enough to transfer all cyclic pitching loads while minimizing assembly size and weight (Fig. 4.4b). Length L_1 was established via the rotor support and is equal to the rotor radius, 9 inches. Length L_4 is equal to the separation distance between the mounting of the rotor radius and pitch link mounting points, 2 inches. Length L_3 , 9.133 in, is the primary pitch link and was designed to bend around the central linear servo. The link was machined out of a sheet of AL 7075 to maximize stiffness and eliminate stress resulting from bent metal manufacturing techniques.

The final length, L_2 , was the most complicated component of the vehicles design. To achieve the desired performance the link assembly must be capable of rotating freely and changing length. The structure of the L_2 link included a machined aluminum bracket which threaded onto a ma-

chined threaded tube. The aluminum assembly serves as the rotational axis for the cyclorotor and is rotated using the rotational servo via a 2:3 gear ratio. The linear servo was used to achieve pitch amplitude control was mounted to the aluminum bracket via a secondary bracket machined from plastic. The presence of the linear servo in the rotational frame means power and signal must be fed through the aluminum bracket and tube via a micro-slip ring before being fed to the vehicles batteries and autopilot. The final pitch mechanism design is a lightweight pitching system which is passively coupled to the rotor's rotation and is capable of independently controlling pitch magnitude and pitch phase.



(a) Schematic



(b) Vehicle

Figure 4.4: Four-bar pitch mechanism: Schematic and vehicle.

4.1.1.3 Blade Design

The span-wise split blade design coupled with the high rotational speeds introduces several structural concerns to ensure durability and functionality. The loads on the blade are split between aerodynamic and centrifugal loads. The contribution of aerodynamic loads to blade deformation is minimal compared to the centrifugal loads. To that end, the blades are designed primarily with concern for the centrifugal loads (Fig. 4.5). The absence of one continuous surface on the blades drastically reduces the overall structural stiffness. The main spar (pitch axis) is the only continuous

structural member and thus served as the primary load path to the side supports (Fig. 4.5d). The two blade halves are free to rotate along this pitch axis. The free rotation of each half of the blades introduces the possibility of pinching between the two blade halves. Along with these concerns, significant effort has been taken at the design stage to minimize blade weight in order to reduce the centrifugal loads.

The blade was designed to allow for maximum structural strength at the lowest possible weight (Fig. 4.5). To accomplish this, each half of the blade is created from three ribs cut from a carbon fiber and foam sandwich structure linked by a filler foam (Fig. 4.5a). The composite material used for the ribs provides a high strength to weight ratio with the only compromise being reduced compressive strength and a laminated structure. To ensure free rotation of each half of the blades in the split blade design a bearing was installed in each rib. Shear forces from the bearing mounted in the rib could delaminate the structure, drastically reducing the structural strength of the rib. A 1mm thick plastic ring was 3D printed and pressed into every rib to provide a mounting surface for the bearings, ensuring loads transferred to the entire rib structure. The filler foam is a rigid low-density Rohacell foam. The foam formed the rigid shape of each half blade and provided a constant surface for mounting the Monokote[®] cover. The foam provides minimal bending strength, so its weight was minimized through the use of the bare amount of material necessary to adhere the Monokote[®] material. To reduce weight the larger leading-edge foam pieces are connected using wooden dowel pins while the trailing edge pieces are held in place with masking tape and minimal epoxy until the Monokote[®] is applied. The assembled blade halves include a 3/16" pultruded carbon fiber rod, that runs through the rear of the half blade (Fig. 4.5b). The rods provide additional structural stiffness as well as the mounting point for the rear pitch control rod. The Monokote[®] wrap creates a clean aerodynamic surface (Fig. 4.5c). The complete blade assembly features the continuous 3/8" pultruded carbon fiber rod along with ABS spacers to position the blades and prevent pinching between the blade halves (Fig. 4.5d). The total blade weight comes in at 0.25 lb (110 g). Despite the added complexity of the split blade design the current blade weight represents one of the lowest ratios of blade weight to blade area achieved from any design to date.

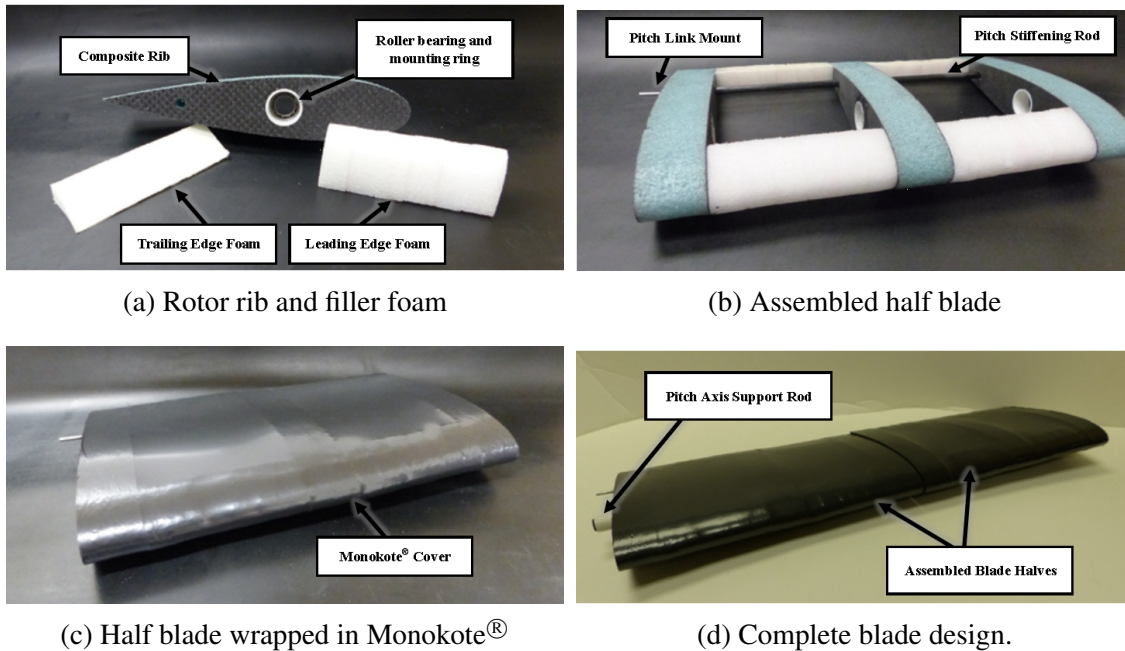


Figure 4.5: Technology demonstrator blade design.

4.1.1.4 Rotor Support Structure and Transmission

The rotor support structure must be designed to handle the large tension loads created by the centrifugal forces on the rotor blades. Despite the lightweight blade design 50 lb of centrifugal force is created by each blade at the operating rotational rate of 850 RPM. To ensure the rotor is capable of handling the large loads with minimal deflection and to minimize rotor weight the supports were machined from an extremely strong laminate composite material (Fig. 4.6). The carbon fiber laminate features a birch core which provides sufficient compressive strength for handling loads while the carbon fiber provided the high tensile strength required to handle the centrifugal forces. The final design includes support arms machined from a 5/32" thick plate of the carbon fiber birch laminate. A central 5/8" radial bearing is pressed and epoxied into the support arms.

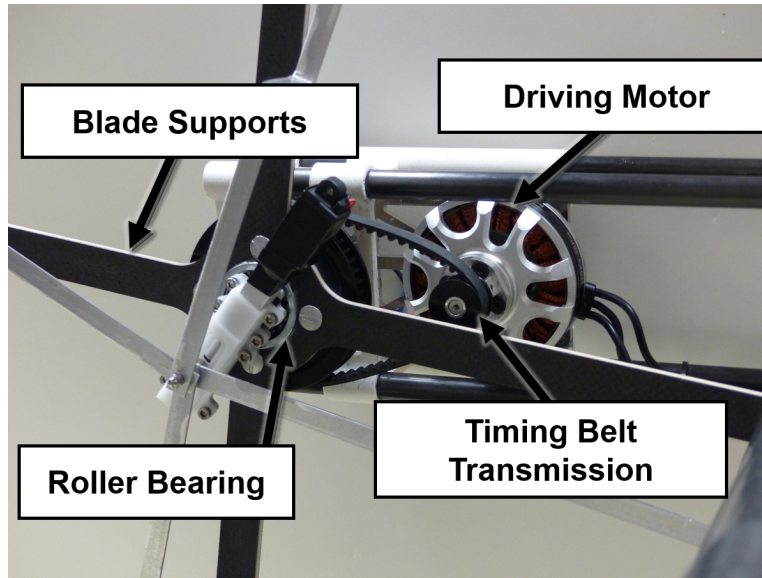


Figure 4.6: Cyclorotor structure and transmission.

Cyclorotors are designed to operate at much lower RPMs than conventional rotors, but at a much higher torque. Current off-the-shelf electric motors are not designed to operate efficiently in these high-torque/low-RPM environments. As such, a transmission system was designed to be mounted directly to the rotor support arms and motor. A timing belt drive system was chosen for the design due to its reduced acoustic signature. The final design featured a 4.17:1 ratio between the pulleys. The driving motor was a 105 kV outrunner KDE motor (KDE10218XF-105) controlled by a 75A KDE speed controller (KDEXF-UAS75HVC). The rotor support structure and transmission system, combined, provided a lightweight design capable of supporting and driving the cyclorotor to necessary operating RPMs.

4.2 Attitude Control Strategy

Achieving stable hovering flight for a novel vehicle concept such as a cyclocopter requires the careful development of attitude control strategies. The current vehicle features 10 independent control mechanisms (2 rotor RPMs, 4 pitch amplitude controls, and 4 pitch phasing controls). The control redundancy present allows for several unique control strategies to be implemented.

The present control strategy is the simplest possible with each control mechanism providing independent control of a degree of freedom. The definition for the vehicles pitch, roll, and yaw

degrees of freedom is provided in Fig. 4.7. The control strategy is detailed in Fig. 4.8 where the thrust vectors are shown for each cyclorotor half. Pitch control is achieved via differential rotor RPM (Fig. 4.8a), i.e. differential rotor thrust, between the front and rear cyclorotor. The direction of rotation of the cyclorotors must be opposite to mitigate inherent pitch moments, but whether both rotors rotate away from or towards the center of the vehicle must be carefully considered. The effect is visualized for a pitch up maneuver in Fig. 4.9. In the case where the rotors are rotating towards the center (Fig. 4.9a), the increase in rotor RPM required to increase the net thrust for the front rotor results in a pitch down reaction torque from the motors. The decrease in rotor RPM for the rear rotor results in a similar pitch down reaction torque. The resulting reaction torque would act against the torque resulting from the thrust differential. In fact, depending on the magnitude of the command input, the rapid response of the reaction torque could cause an initial pitch down followed by a pitch up. However, if the cyclorotors were rotated away from the center, as they are on the current vehicle, the reaction torque would be reversed causing the reaction torque and thrust differential to work together resulting in an increase in responsiveness (Fig. 4.9b). Roll control relies on differential pitch amplitudes, i.e. differential rotor thrust, between the left and right halves of the vehicle (Fig. 4.8b). Yaw control is obtained by vectoring the thrust in opposite directions between the right and left halves of the vehicle (Fig. 4.8c). The current control strategy minimizes coupling from commanded inputs. Vehicle trim is accomplished initially via geometric positioning of the blade-pitch control length. Additional vehicle trim is achieved during the flight-testing process.

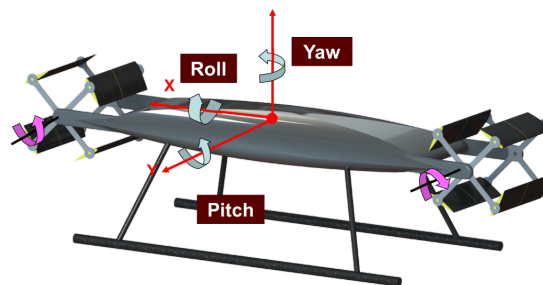


Figure 4.7: Control definitions.

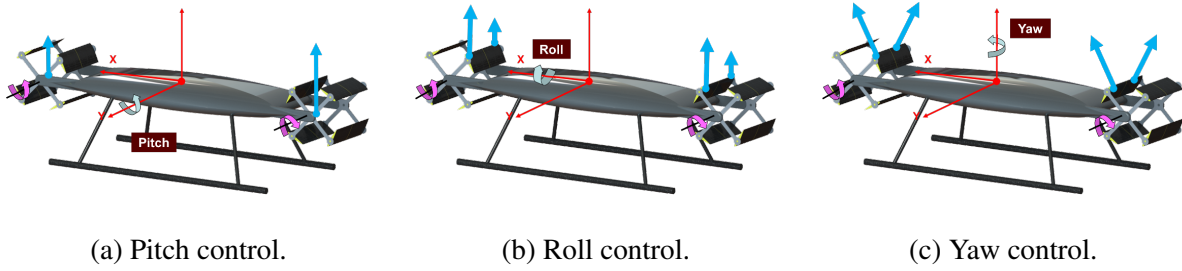


Figure 4.8: Attitude control strategy.

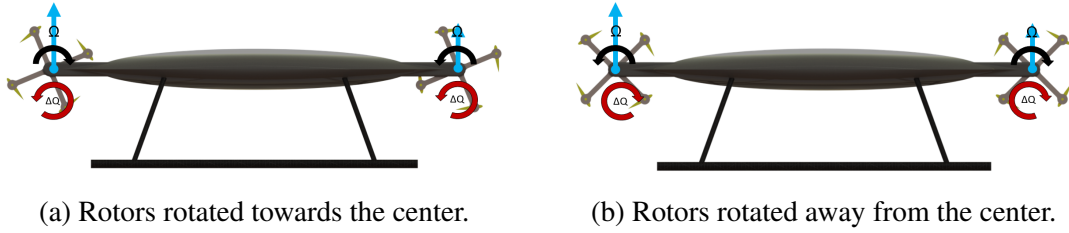


Figure 4.9: Motor reaction torques effect on pitch stability. Pitch up maneuver represented.

4.2.1 Avionics and Feedback Control

A feedback control system is required to provide sufficient attitude damping and stiffness to achieve stable hover. A state-of-the-art inertial navigation system was incorporated into the vehicle to handle the onboard processing necessary. The navigation system known as ELKA-R (Embedded Lightweight Kinematic Autopilot-Revised) was developed at the University of Maryland [35]. The board features a 32-bit low-power ARM Cortex-MR microprocessor and is capable of stabilization rates as high as 1000 Hz. 2.4 GHz XBEE and PPM receivers were installed to handle communication of control inputs from the remote as well handle communication of telemetry data to a computer via LabVIEW for active recording. The telemetry connection also provides a means to actively update the vehicles feedback gains and trim inputs.

The on-board gyros measure the pitch (q), roll (p) and yaw (r) angular rates while the accelerometers record the tilt of the gravity vector in the body frame. The vehicle attitude can then be extracted by integrating the gyro measurements with time. However, it is known that this leads to drift in attitude measurements. Accelerometers on the other hand offer stable bias but are sensitive to vibrations and in general offer poor high frequency information. Therefore, a complementary filter was incorporated to extract the pitch and roll Euler angles using a high-

pass filter for the gyros (4 Hz cut-off) and a low-pass filter for accelerometers (6 Hz cut-off). The rotational vibrations were filtered out since they are sufficiently higher than the body dynamics. On-board inner loop feedback was implemented using a proportional-derivative (PD) controller as shown in Fig. 4.10. The feedback states are the pitch and roll Euler angles θ and ϕ and the attitude rates, p , q and r . The outer loop feedback capability was provided for translational positioning by a human pilot or for a position tracking system.

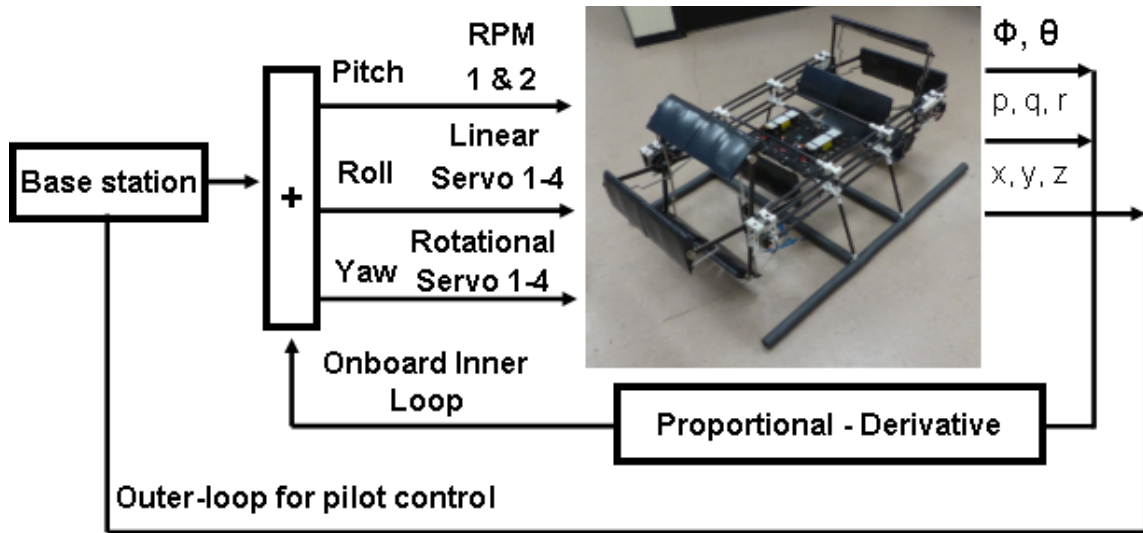


Figure 4.10: Feedback loop.

4.3 Experimental Testing

Prior to the initiation of flight-testing gimbal testing and tethered flight testing was conducted as a means to verify proper operation of all mechanical and electrical systems. Gimbal testing involved mounting the vehicle through a spherical bearing allowing for three rotational degrees of freedom, namely, pitch, roll and yaw (Fig. 4.11). Conducting experiments on the gimbal test stand was a crucial step to flight testing as a means for troubleshooting with minimal risk to the vehicle. Systematic tests allowed for the determination of the gains necessary to achieve acceptable stiffness and damping to reject external disturbances with minimal oscillations.



Figure 4.11: Gimbal test stand.

Following gimbal tests, tethered flight tests were conducted to verify vehicle liftoff and control responsiveness (Fig. 4.12). Slight modifications to the feedback gains were determined necessary to account for the change in point of rotation (center of gravity vs center of spherical bearing) and removal of friction from the bearing. Tethered flight tests demonstrated stability in pitch and yaw, but also showed that the vehicle lacked the responsiveness in roll necessary to maintain stable hovering flight due to the slow response of the linear servos responsible for controlling pitch amplitude. To rectify the problem the linear servos were changed from the L12 Actuonix servo with a 210:1 gear ratio to the L16 63:1 gear ratio. The servo replacement provided similar strength with a three-fold increase in speed at the cost of a 20 gram increase per servo.

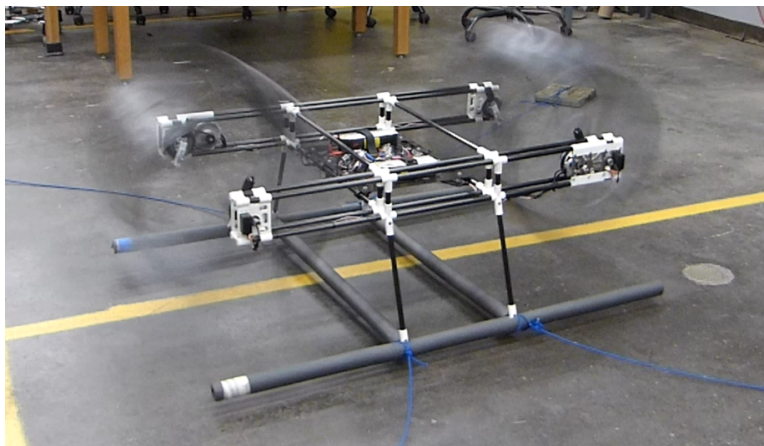


Figure 4.12: Tethered flight test

Following the integration of the new linear servos free flight tests were conducted. Flight tests with zero gains demonstrated the need to carefully trim the vehicle to maximize control performance and prevent unwanted translational movement. Following trim flights the gains were carefully tuned through a series of systematic flight tests. Free flights have demonstrated continued stability in pitch and yaw, but roll instabilities persist at a reduced magnitude compared to those prior to the servo replacement. Limited periods of stable hover were achieved as shown in Fig. 4.13.



Figure 4.13: Free flight test

4.4 Concluding Remarks

This chapter presents the development of a VTOL-capable, UAV-scale cyclocopter, with a gross weight of 17 pounds. The vehicle features a dual-rotor configuration with one cyclorotor positioned at the front and the other at the rear of the vehicle. The rotors feature a novel split-blade design. Each rotor is capable independent control of the pitch amplitude and phase of each blade half. The independent pitch kinematics of each blade half allows each cyclorotor to operate like two rotors operating at the same rotational rate. The current attitude control strategy uses a combination of differential RPM between the front and rear rotors, differential pitch amplitude between the left and right halves of the rotors, and differential cyclic pitch phase between the left and right halves of the rotor for pitch, roll, and yaw control. The vehicle was demonstrated through gimbal, tethered and free flight tests and showed pitch and yaw stability with minor roll instabilities which are actively being addressed.

5. SUMMARY AND CONCLUSIONS

This thesis discusses the experimental optimization of a UAV-scale cyclorotor's aerodynamic performance through an extensive experimental parametric study and the creation of a UAV-scale cyclocopter. The experimental parametric study was conducted using a custom three-component balance developed in-house to measure time-averaged forces, torque and rotational speed of a UAV-scale cyclorotor prototype. The cyclorotor prototype was tested with varying cyclic pitch amplitudes (symmetric and asymmetric), blade airfoil thicknesses, blade spans, chord-by-radius ratios, blades numbers, and solidities. By carefully examining the thrust and power measurements for each rotor configuration a series of guidelines were established for the design of an optimized cyclorotor. To demonstrate the flight worthiness of the design, a UAV-scale cyclocopter was created. The 17 lbs demonstration vehicle featured a dual-rotor configuration with one cyclorotor positioned at the front and the other at the rear of the vehicle. Each cyclorotor featured a novel split-blade design and was aerodynamically optimized using lessons learned from the parametric study. The vehicle was demonstrated through gimbal, tethered and free flight tests and showed pitch and yaw stability with minor roll instabilities which are actively being addressed.

Specific conclusions from the experimental parametric study include:

1. A state-of-the-art hover stand featuring a three-component balance was constructed to measure a UAV-scale cyclorotor's vertical thrust (T_Z), sideward thrust (T_Y), aerodynamic torque (Q), and rotational speed.
2. The cyclorotor geometry significantly affects the optimal pitch amplitude due to variation in the flow curvature effect, which introduces a dynamic virtual camber to the blades and rotor inflow, which changes the effective angle of attack of the blades.
3. Contrary to results found during previous MAV-scale studies, asymmetric pitching was found to provide no appreciable performance benefits in terms of aerodynamic efficiency, quantified in terms of power loading.

4. Increasing the airfoil thickness from 15% up to 25% for a symmetric NACA airfoil resulted in minimal change in the peak power loading achieved. However, increasing the thickness did increase the range of pitch amplitudes over which the cyclorotor was able to maintain a high-power loading, which would enable expanded regimes of efficient operation.
5. Increasing the blade span or blade aspect ratio resulted in minimal change in thrust per unit area, power per unit area or power loading values. Coupled with experiments utilizing endplates it is assumed the cyclorotors exhibits minimal changes in 3-D flow or tip losses for small aspect ratios ($AR < 5$).
6. Optimal chord-by-radius ratios were found to fall between 0.5 and 0.66 when considering thrust per unit blade area (C_T/σ). When considering power loading, the optimal chord-by-radius ratio was 0.66. Increasing the chord-by-radius ratio beyond 0.66 was found to decrease C_T/σ and power loading.
7. The blades produced decreasing thrust per unit area with increasing number of blades. This was in part due to increased blade interactions and in part to the reduced effective angles of attack of the blades with increased inflow (or increased thrust) for a fixed blade speed.
8. Increasing number of blades had varying impacts on the cyclorotor power loading depending on chord-by-radius ratio and solidity.
9. The optimal rotor solidity (blade area/swept area) falls between 0.3 and 0.4. Both from thrust per unit blade area and power loading standpoints, it is much more advantageous to increase rotor solidity by increasing chord/radius rather than number of blades (with small chord-by-radius ratio) so long as the chord-by-radius ratio does not exceed 0.7.
10. The peak figure of merit demonstrated for a UAV-scale cyclorotor is 0.6 at $Re=200,000$. The respective rotor configuration and one represented for the design of an optimal cyclorotors features a chord-by-radius ratio of 0.66, 3 blades featuring a blade aspect ratio (span/chord)

of 4 and a NACA 0020 airfoil, rotor aspect ratio (span/diameter) of 1.33 and pitch amplitude of 40 deg.

Specific conclusions from the development of the UAV-scale demonstration vehicle include:

1. The results from the parametric study were levered to create an aerodynamically optimized cyclorotor for the demonstration vehicle. The rotors feature a 6 in blade chord, 18 in rotor diameter, and 18 in blade span. The 18 in blade span is divided equally between two 9 in blade halves featuring NACA 0020 airfoils with nominal pitch amplitudes of $\pm 35^\circ$.
2. A compact and mechanically simple pitch mechanism was created using a four-bar linkage system. The central control links length and radial position was varied independently by linear and rotational servos providing both pitch amplitude and phase control for each blade half.
3. Independent control of each cyclorotors RPM and each blade halves pitch amplitude and phase introduced redundancy into the control system. The present attitude control strategy relies on differential RPM between the two cyclorotors for pitch control, differential pitch amplitude between the blade halves for roll control and differential cyclic pitch phase between the blades halves for yaw control.
4. Present gimbal, tethered flight tests, and free flight tests demonstrated sufficient control authority exists in pitch, roll and yaw. Current limitations in mechanical response rate minimize roll damping resulting in roll instabilities.

5.1 Future Work

Compared to conventional rotors, cyclorotors are still in their early stages of development with a plethora of areas available for study. Previous studies have focused on developing a complete understanding of the aerodynamics of MAV-scale cyclorotors and the implementations of the rotors on cyclocopters. At the UAV-scale one cyclocopter was successfully demonstrated in free flight

and a collection of analytical studies were conducted, but none of the studies involved a systematic approach to understand the rotors aerodynamics and its affect on the performance. This thesis provided one of the first detailed experimental studies on the hover performance of UAV-scale cyclorotors and demonstrated a unique split-blade rotor design on a vehicle.

As an extension to the current study, particle image velocimetry (PIV) studies are required for further understanding for the aerodynamics. One specific area of interest would be span-wise imagery used to examine the formation of tip vortices and how it changes with changing aspect ratio. PIV results would also prove beneficial in the validation of future CFD analysis of UAV-scale cyclorotors.

Experimentally, the forward flight performance of UAV-scale cyclorotors needs to be investigated. The complex nature of a cyclorotor's curvilinear geometry means there could be a significant change in the optimal rotor design depending on desired forward speed. The experimental study should investigate the affect of pitch kinematics as well as rotor geometry. Systematic PIV studies should be conducted along with the parametric performance study.

A holistic computational study should be conducted on UAV-scale cyclorotors to understand the true scalability of the concept. Relying on the experimental data presented in this thesis lower order aerodynamic models can be developed and verified. The model can than be used to determine optimal rotor configurations that may have been overlooked during the experimental study. The analytical results should be combined with a coupled CFD-CSD aeroelastic analysis to develop a true understanding for the aerodynamic phenomena present.

To further the development of future cyclocopters, new vehicle concepts and control strategies must be investigated. Improvements for the current technology demonstrator would include the improvement of both roll response rate, through improved servos with reduced deadband and increased travel rates, and roll control authority, through modified blade design (increased blade span). In addition to more complex feedback controller designs the vehicle's stability could be improved by using different control strategies which utilize new combinations of pitch amplitude, pitch phase, and RPM modulation to achieve stability.

REFERENCES

- [1] “Cyclogyro history.” [Online]. Available: http://rotoplan.narod.ru/history_e.htm
- [2] K. Kirsten, U.S. Patent 1 432 700, October 17, 1922.
- [3] H. Sachse, “Kirsten-Boeing Propeller,” National Advisory Committee for Aeronautics, Tech. Rep., Feb. 1926.
- [4] S. Elonka, “Development of cycloidal propeller,” *Marine Engineering and Shipping Review*, vol. 51, no. 6, pp. 110–113, 1946.
- [5] C. B. Strandgren, “The Theory of the Strandgren Cyclogiro,” National Advisory Committee for Aeronautics, Tech. Rep., Jul. 1933.
- [6] J. Wheatley, “Simplified aerodynamic analysis of the cyclogiro rotating-wing system,” National Advisory Committee for Aeronautics, Tech. Rep., 1933.
- [7] ———, “Wind-tunnel tests of a cyclogiro rotor,” National Advisory Committee for Aeronautics, Tech. Rep., May 1935.
- [8] J. Boschma and M. McNabb, “Cycloidal Propulsion for UAV VTOL Applications,” Naval Air Warfare Center-Aircraft Division, Tech. Rep., 1998.
- [9] J. Boschma, “Modern Aviation Applications for Cycloidal Propulsion,” in *AIAA Aircraft, Technology Integration, and Operations Forum Proceedings*, Los Angeles, CA, Oct. 16-18, 2001.
- [10] C. Runco, D. Coleman, and M. Benedict, “Development of the World’s Smallest Cyclocopter,” in *72nd Annual National Forum of the American Helicopter Society*, West Palm Beach, FL, May 17-19, 2016.
- [11] M. Benedict, E. Shrestha, V. Hrishikeshavan, and I. Chopra, “Development of a 200 gram Twin-Rotor Micro Cyclocopter Capable of Autonomous Hover,” in *American Helicopter Society Future Vertical Lift Aircraft Design Conference*, San Francisco, CA, Jan. 18-20, 2012.

- [12] M. Benedict, J. Mullins, V. Hrishikeshavan, and I. Chopra, "Development of a Quad Cycloidal-Rotor Unmanned Aerial Vehicle," *Journal of the American Helicopter Society*, vol. 61, pp. 1–12, Apr. 2016.
- [13] M. Benedict, T. Jarugumilli, and I. Chopra, "Effect of Rotor Geometry and Blade Kinematics on Cycloidal Rotor Hover Performance," *Journal of Aircraft*, vol. 50, no. 5, pp. 1340–1352, Sep. 2013.
- [14] —, "Experimental Optimization of MAV-Scale Cycloidal Rotor Performance," *Journal of the American Helicopter Society*, vol. 56, no. 2, pp. 1–11, Apr. 2011.
- [15] M. Benedict, M. Ramasamy, I. Chopra, and J. G. Leishman, "Performance of a Cycloidal Rotor Concept for Micro Air Vehicle Applications," *Journal of the American Helicopter Society*, vol. 55, no. 2, pp. 1–14, Apr. 2010.
- [16] M. Benedict, M. Ramasamy, and I. Chopra, "Improving the Aerodynamic Performance of Micro-Air-Vehicle-Scale Cycloidal Rotor: An Experimental Approach," *Journal of Aircraft*, vol. 47, no. 4, pp. 1117–1125, Aug. 2010.
- [17] A. H. Lind, T. Jarugumilli, M. Benedict, V. K. Lakshminarayan, A. R. Jones, and I. Chopra, "Flow Field Studies on a Micro-Air-Vehicle-Scale Cycloidal Rotor in Forward Flight," *Experiments in Fluids*, vol. 55, pp. 1–17, Nov. 2014.
- [18] M. Benedict, T. Jarugumilli, V. K. Lakshminarayan, and I. Chopra, "Effect of Flow Curvature on the Forward Flight Performance of a MAV-Scale Cycloidal Rotor," *AIAA Journal*, vol. 52, no. 6, pp. 1159–1169, Jun. 2014.
- [19] T. Jarugumilli, M. Benedict, and I. Chopra, "Wind Tunnel Studies on a Micro Air Vehicle-Scale Cycloidal Rotor," *Journal of the American Helicopter Society*, vol. 59, no. 2, pp. 1–10, Apr. 2014.
- [20] S. Elena, V. Hrishikeshavan, M. Benedict, D. Yeo, and I. Chopra, "Development of Control Strategies for a Twin-Cyclocopter in Forward Flight," *Journal of the American Helicopter Society*, vol. 61, no. 4, pp. 1–9, Oct. 2016.

- [21] C. Runco, D. Coleman, and M. Benedict, "Design and Development of a Meso-Scale Cyclocopter," in *AIAA SciTech*, San Diego, California, Jan. 4-8, 2016.
- [22] S. Hwang, S. Min, M. Kim, and S. Kim, "Multidisciplinary Optimal Design of Cyclocopter Blade System," in *46th AIAA/ASME/ASCE/AHS/ASC Structures, Structural Dynamics & Materials Conference*, Austin, TX, Apr. 18-21, 2005.
- [23] S. Hwang, S. Min, C. Lee, and S. Kim, "Experimental Investigation of VTOL UAV Cyclocopter with Four Rotors," in *48th AIAA/ASME/ASCE/AHS/ASC Structures, Structural Dynamics & Materials Conference*, Honolulu, Hawaii, Apr. 23-26, 2007.
- [24] I. S. Hwang, S. Y. Min, C. H. Lee, and S. J. Kim, "Development of a Four-Rotor Cyclocopter," *Journal of Aircraft*, vol. 45, no. 6, pp. 2151–2157, Nov. 2008.
- [25] C. H. Lee, S. Y. Min, J. W. Lee, and S. J. Kim, "Design and Experiment of Two-Rotored UAV Cyclocopter," in *29th Congress of the International Council of the Aeronautical Sciences*, St. Petersburg, Russia, Sep. 7-12, 2014.
- [26] "Cyclocopter demonstration." [Online]. Available: <https://www.youtube.com/watch?v=gbn0Bnt3iDs>
- [27] "Oran w. nicks low speed wind tunnel." [Online]. Available: <https://lswt.tamu.edu>
- [28] A. Kellen and M. Benedict, "Performance Measurements of UAV-Scale Cycloidal Rotor," in *73rd Annual National Forum of the American Helicopter Society*, Fort Worth, TX, May 9-11, 2017.
- [29] —, "Experimental Optimization of UAV-Scale Cycloidal Rotor Performance," in *Proceedings of the AHS Technical Conference on Aeromechanics Design for Transformative Vertical Flight*, San Francisco, CA, Jan. 16-19, 2018.
- [30] —, "Effect of Rotor Geometry on UAV-Scale Cycloidal Rotor Hover Performance," in *74th Annual National Forum of the American Helicopter Society*, Phoenix, AZ, May 14-17, 2018.

- [31] T. Jarugumilli, M. Benedict, and I. Chopra, “Experimental Optimization and Performance Analysis of a MAV Scale Cycloidal Rotor,” in *AIAA Aerospace Sciences Meeting*, Orlando, FL, Jan. 4-7, 2011.
- [32] C. Walther and M. Benedict, “Experimental and Computational Studies to Understand Unsteady Aerodynamics of Cycloidal Rotors in Hover at Ultralow Reynolds Numbers,” in *73rd Annual National Forum of the American Helicopter Society*, Fort Worth, TX, May 9-11, 2017.
- [33] A. Halder, C. Walther, and M. Benedict, “Unsteady Hydrodynamic Modeling of a Cycloidal Propeller,” in *Fifth International Symposium on Marine Propulsion*, Helsinki, Finland, Jun. 12-15, 2017.
- [34] A. Kellen, J. White, and M. Benedict, “Development of a UAV-Scale Cyclocopter,” in *Proceedings of the Autonomous VTOL Technical Meeting and Electric VTOL Symposium*, Mesa, AZ, Jan. 29-31, 2019.
- [35] V. Hrishikeshavan and I. Chopra, “Refined lightweight inertial navigation system for micro air vehicle applications,” *International Journal of Micro Air Vehicles*, vol. 9, no. 2, pp. 124–135, Jun. 2017.